



**HAL**  
open science

# High Reynolds number unsteadiness assessment using 3D and 2D computational fluid dynamics simulations of a thick aerofoil equipped with a spoiler

Thomas Potentier, Emmanuel Guilmineau, Arthur Finez, Colin Le Bourdat,  
Caroline Braud

## ► To cite this version:

Thomas Potentier, Emmanuel Guilmineau, Arthur Finez, Colin Le Bourdat, Caroline Braud. High Reynolds number unsteadiness assessment using 3D and 2D computational fluid dynamics simulations of a thick aerofoil equipped with a spoiler. *Wind Energy*, 2023, 26 (7), pp.668-690. 10.1002/we.2823 . hal-04281929

**HAL Id: hal-04281929**

**<https://hal.science/hal-04281929v1>**

Submitted on 14 Nov 2023

**HAL** is a multi-disciplinary open access archive for the deposit and dissemination of scientific research documents, whether they are published or not. The documents may come from teaching and research institutions in France or abroad, or from public or private research centers.

L'archive ouverte pluridisciplinaire **HAL**, est destinée au dépôt et à la diffusion de documents scientifiques de niveau recherche, publiés ou non, émanant des établissements d'enseignement et de recherche français ou étrangers, des laboratoires publics ou privés.

## RESEARCH ARTICLE

WILEY

# High Reynolds number unsteadiness assessment using 3D and 2D computational fluid dynamics simulations of a thick aerofoil equipped with a spoiler

Thomas Potentier<sup>1,2</sup>  | Emmanuel Guilmineau<sup>1</sup> | Arthur Finez<sup>3</sup> |  
Colin Le Bourdat<sup>2</sup> | Caroline Braud<sup>1</sup>

<sup>1</sup>LHEEA (Centrale Nantes / CNRS), Nantes, France

<sup>2</sup>ENGIE Green, Nantes, France

<sup>3</sup>ENGIE Green, Lyon, France

## Correspondence

Thomas Potentier, LHEEA (Centrale Nantes / CNRS), 1 rue de la Noë, 44321 Nantes Cedex 3, France.

Email: [thomas.potentier@gmail.com](mailto:thomas.potentier@gmail.com)

## Funding information

Association Nationale de la Recherche et de la Technologie, Grant/Award Number: 2019/1426; Grand Equipement National de Calcul Intensif, Grant/Award Number: A0112A13014

## Abstract

An operating 2-MW wind turbine has been scanned and analysed using 2D computational fluid dynamics (CFD) and blade element momentum (BEM) analysis. The current work illustrates using full-scale 3D CFD simulations the differences between 2D and 3D simulations and its impact on the local aerofoil vortex shedding frequency. The outcome shows that despite a pressure redistribution and lift change introduced by the blade span and rotation, the vortex shedding frequency remains similar between 2D and 3D thereby validating the novel fatigue calculation method previously proposed.

## KEYWORDS

aerodynamics, spoiler, unsteadiness, vortex shedding frequency, wind turbine

## 1 | INTRODUCTION

Over the last 40 years, the average temperature increased by 2.2°C in Europe, with dire consequences for the inhabitants, for example, flood and fire. In December 2019, the European Union (EU) agreed to fight climate change and global warming by becoming “climate-neutral” by 2050. To achieve this goal, several milestones have been set, one of them is “Fit for 55.” This programme should enable each country to halve its carbon emission (compared to 1990 levels). Several actions including energy efficiency or alternative fuels have been put forward by the EU. The share of renewable energy in the energy mix should also increase to 40% by 2030. Among the possible renewable energy sources is the wind energy (both onshore and offshore). The recent developments in turbine design allowed turbine manufacturers to be competitive on the electricity market. The Levelized Cost of Energy (LCoE<sup>\*</sup>) of wind (onshore and offshore) is within the production cost of coal since 2010 according to IRENA's report.<sup>1</sup>

In order to remain competitive on the energy market, wind turbine manufacturers have to keep innovating to overcome some design constraints. Intrinsically, a blade, by its shape, imposes a thick (cylinder like) shape towards the root to withstand the loads and thinner outboard where most of the energy is generated. Despite being mandatory from a structural point of view, this design is detrimental for the energy production. There exists several types of device that are meant to overcome the blade design limitations or reduce the acoustic emission. Such devices are called Aerodynamic Add-Ons (AAO); a vast literature already exists and will not be detailed here.<sup>2–4</sup> AAOs are mainly installed at the blade root for power increase (e.g., Gurney flap and vortex generator) and at the blade outboard for reducing the noise (e.g., serrations). AAOs add a

\*Measure of the average net present cost of electricity generation for a generating plant over its lifetime.

This is an open access article under the terms of the [Creative Commons Attribution-NonCommercial-NoDerivs](https://creativecommons.org/licenses/by-nc-nd/4.0/) License, which permits use and distribution in any medium, provided the original work is properly cited, the use is non-commercial and no modifications or adaptations are made.

© 2023 The Authors. *Wind Energy* published by John Wiley & Sons Ltd.

non-negligible Capital Expenditure cost (CAPEX<sup>†</sup>) requiring a solid business case for the exploiting party, despite increasing the overall energy production.<sup>5–7</sup>

With the increased rotor diameter and hub height, turbine manufacturers are now facing aeroelastic challenges where tower and blades can deform over large distances. Larger blades require more attention to details during the design phase to reduce the cost. The maintenance cost during the turbine lifetime increases too; a good understanding of the turbine ageing is necessary. During routine maintenance, ENGIE Green, an exploiting party, noticed that some turbines equipped with a specific root AAO presented cracks. The AAO is the canoe-spoiler or *spoiler* and is installed between the radial position 3 m from the blade root until 7.5 m. The material initially chosen to build the spoiler may be too stiff leading to stress concentration and facilitating the cracks appearance. However, some aerodynamic phenomena unaccounted for in the design could be at play and will be investigated here.

Previous studies were dedicated to develop a method to estimate fatigue loading introduced by root spoilers, or add-ons in general, from 2D computational fluid dynamics (CFD) simulations and blade element momentum (BEM) aeroelastic simulations.<sup>8,9</sup> The present paper focuses on estimating differences between 2D and 3D CFD flow physics at the root spoiler and ultimately ensures the correctness of the method previously introduced.<sup>9</sup> It will be performed by comparison and quantification of the spoiler unsteadiness impact onto a wind turbine blade. Each case (no spoiler and spoiler) will be analysed using state-of-the-art 3D CFD unsteady Reynolds averaged Navier–Stokes (URANS) solver: ISIS-CFD.<sup>10–12</sup> The present simulations do not include the full turbine geometry (no tower and no nacelle) and consider rigid blades. The inflow is simplified to a steady and uniform case. Only one operating condition is simulated and chosen from the optimization procedure presented in Potentier et al.<sup>9</sup> The results presented after are limited to the following operating conditions:

- Inflow: 8 m/s
- Pitch:  $-1.568^\circ$
- Rotation speed: 14.1 RPM

At last, results from the root spoiler configuration are systematically presented against simulations of the no spoiler configuration for comparison purposes. Results are separated in two parts. The first part presents results at the rotor scale including two sections. The first section gives an overview of the far wake organization. In the following section, the zone impacted by the spoiler is presented. In the second section, results focus on the blade aerodynamics. First, the 3D blade flow organization will be analysed to end with unsteady pressure distribution in the blade root area.

Because of the blade scan orientation and CFD set-up (see Figure 1C), the main velocity is following the z-axis ( $U_z$ ), the x-axis represents the chordwise velocity ( $U_x$ ) and the y-axis the spanwise velocity ( $U_y$ ).

## 2 | ROTOR DESCRIPTION

The wind turbine geometry used in the present thesis was acquired during a scanning campaign organized by Maïa Eolis (former ENGIE Green) as part of a master thesis project.<sup>13</sup> Several steps are taken to ensure that the smoothing of the cloud point does not distort the geometry and four different high-order Bezier splines are used to fit through the cloud of point (not presented here). Thanks to the scan post-process, the blade geometry was extracted. The turbine radius,  $R$ , is 45 m long and is equipped with a root spoiler from the radial position  $r/R = 0.07$  until  $r/R = 0.17$ . Figure 1 shows the pressure side of the rotor (Figure 1A) and a zoom-in area located at the radial position  $R6$ , equivalent to  $r/R = 0.13$ , (Figure 1B).

## 3 | MESH SENSITIVITY STUDY

### 3.1 | ISIS-CFD

ISIS-CFD, developed by Centrale Nantes and CNRS and available as a part of the FINE™/Marine computing suite, is used in the present thesis to solve the incompressible URANS equations. It is based on the finite volume method to build the spatial discretization of the transport equations. The unstructured discretization is face-based, which means that cells with an arbitrary number of arbitrarily shaped faces are accepted (producing thus an *unstructured mesh*), as illustrated in Figure 2. A second-order backward difference scheme is used to discretize time. The solver can simulate both steady and unsteady flows. In the case of turbulent flows, transport equations for the variables in the turbulence model are added to the discretization.

<sup>†</sup>Funds used by a company to acquire, upgrade, and maintain physical assets such as property, plants, buildings, technology, or equipment.

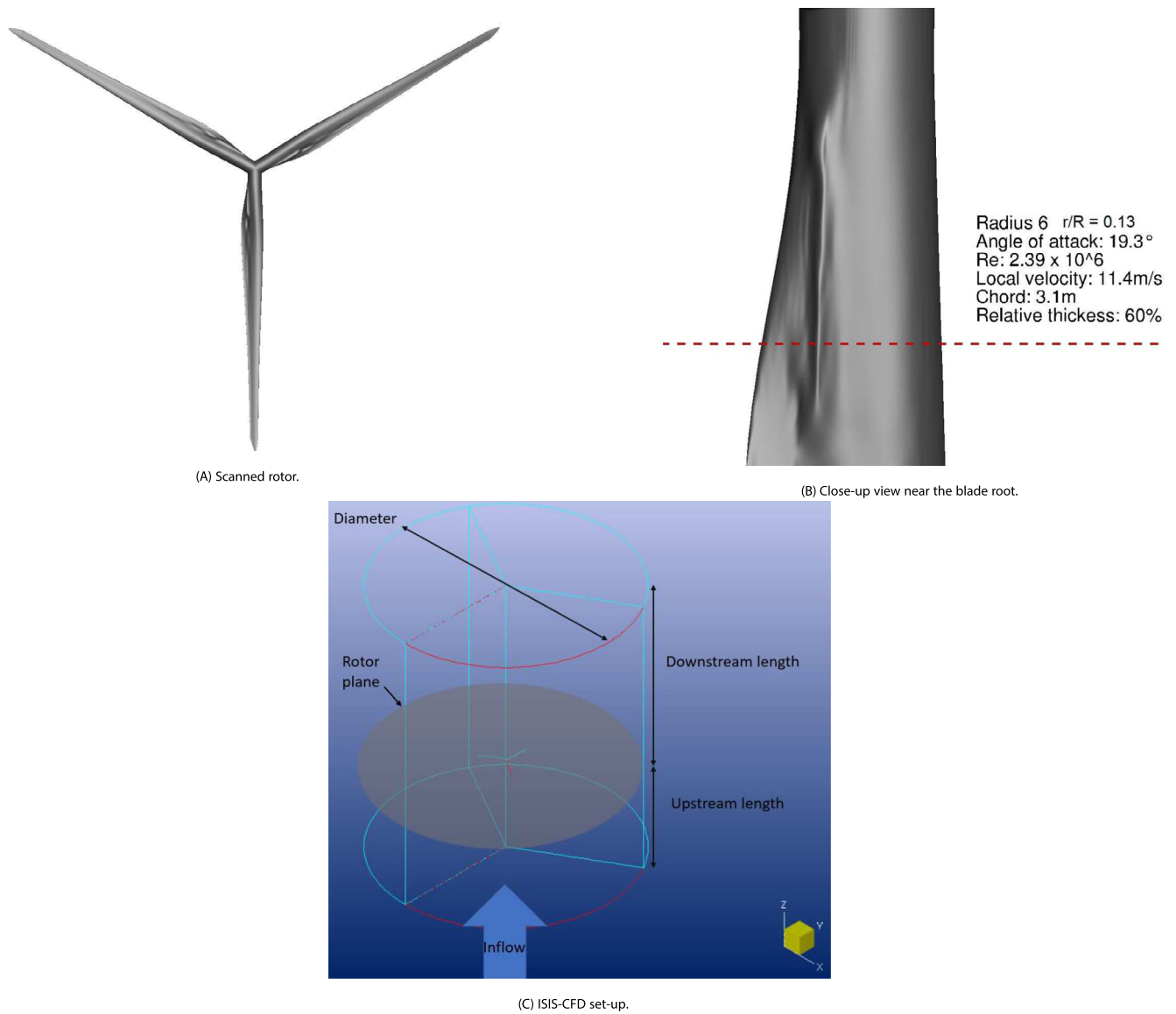


**FIGURE 1** Rotor and coordinate system illustration.

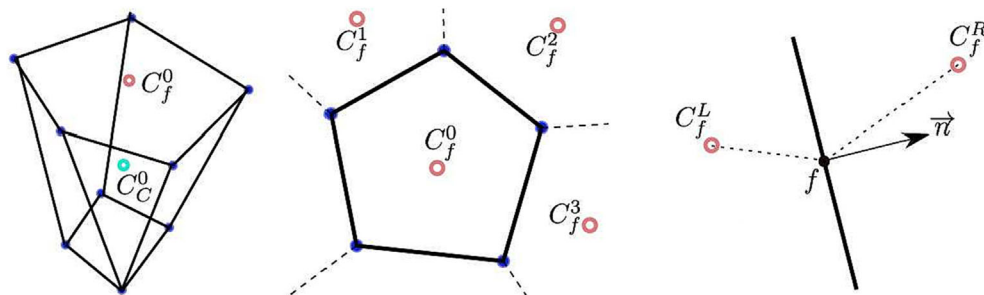


**FIGURE 2** Generic unstructured mesh. Left: Typical unstructured control volume. Middle: Cell  $C^0$  and its neighbour cells. Right: Centred face reconstruction notations.

All flow variables are stored at the cells geometric centre. Volume and surface integrals are evaluated with second-order accurate approximations. The method is face-based, which means that the net fluxes in the cells are computed face by face. Numerical fluxes are reconstructed on the mesh faces by linear extrapolation of the integrand from the neighbouring cell centres. A centred scheme is used both for the diffusion terms

and convective fluxes. The velocity field is obtained from the momentum conservation equations and the pressure field is extracted from the mass equation constraint, or continuity equation, transformed into a pressure equation. The pressure equation is obtained by the Rhie and Chow interpolation.<sup>14</sup> The momentum and pressure equations are solved in a segregated manner as in the SIMPLE coupling procedure.<sup>15</sup> ISIS-CFD refinement routine automatic grid refinement (AGR) allows for cell count reduction in the mesh by refining only where necessary based on the several user defined criteria.<sup>16,17</sup>

### 3.2 | Domain definition

The work performed using the known reference of the DANAERO blade project allowed to highlight the calculation domain boundaries as well as the blade discretization.<sup>18</sup> It also showed that activating the automatic grid refinement enabled a cell count reduction while maintaining a high fidelity results. Table 1 shows the used domain size.

Figure 3A shows the full calculation domain. Figure 3B–D shows a zoomed-in view of the mesh around a single blade and the rotor.

### 3.3 | Mesh independence results

Each case is run three times: One run without refinement and two AGR configurations (Refinement 1 and Refinement 2). The refinement criterion thresholds are 9 and 4.5 m, corresponding to the reference length (blade radius) divided by 5 and 10, respectively, and the minimum cell size is 0.1 m. The time step is kept constant during the simulations and taken to be  $\Delta t = 0.01$ s, which is equivalent to a rotation of  $2^\circ$  per time step.

Due to time constraints, the rotor simulations were limited, and in particular, it does not include the nacelle and the tower. Also, the wind inflow was considered uniform and steady in the overall 3D simulation. At last, only one operational condition was performed with and without spoiler. The presented results show the simulations outcome for an operating wind speed of 8 m/s and a pitch settings of  $-1.568^\circ$  following the pitch setting optimization.<sup>9</sup> The chosen wind speed is in the part II of the power curve; that is, the turbine is operating at its optimal power coefficient (here the power coefficient is approximately 0.42).

Tables 2 and 3 show the impact of the AGR on the aerodynamic thrust. The load is almost equal both for the “Refinement 1” and “Refinement 2,” while the cell count and calculation time are drastically increased with the highest refinement. Therefore, for the rest of the paper, only the “Refinement 1” results will be used.

## 4 | AT THE ROTOR SCALE

In this section, the impact of the spoiler is analysed for the first time using 3D URANS simulations. The first section gives a description of the spoiler effect at the rotor scale: Upstream in the induction zone, downstream in the rotor near and far wake area, and finally in the rotor plane (the axial and tangential induction and the angle of attack). Major impacts are expected in the blade root area and are detailed later. The impacted area is first identified using the mean wall shear stress quantity; then the blade root mean flow organization is described. The loads associated to the spoiler addition are analysed by means of the pressure coefficient and lift coefficient ( $C_p$  and  $C_L$ , respectively). Finally, the unsteady flow and loads are characterized using spectrum analysis.

The following table highlights the main operating conditions for the 3D simulations at  $r/R = 0.13$ .

### 4.1 | Upstream and downstream the rotor

The upstream region of the turbine is dominated by the induction zone. It is defined by the wind inflow reduction when approaching the turbine. The induction zone is defined here where the velocity is below 99% of the inflow. In Figure 4, the rotor centre of rotation is located in  $[X/D=0; Y/D=0; Z/D=0]$ , where X, Y, and Z are the Cartesian coordinate system used, the rotor plane being located in the X–Z plane. The

**TABLE 1** Domain size.

Case	Diameter (m)	Upstream length (m)	Downstream length (m)	Blade length (m)
No spoiler	4000	800	800	45
Spoiler	4000	800	800	45

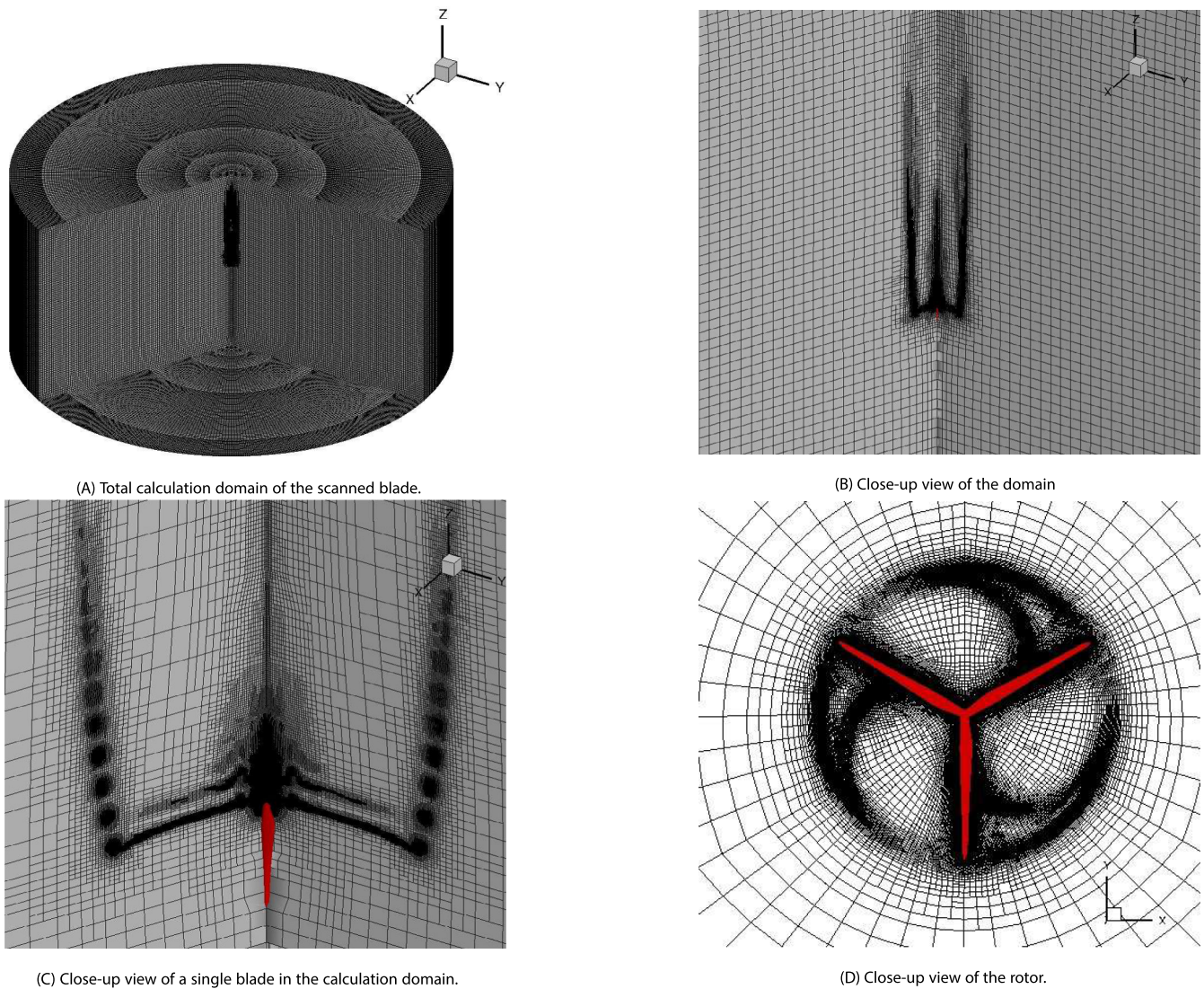


**FIGURE 3** Different views of the scanned blade in its calculation domain.

**TABLE 2** Comparison of the aerodynamic thrust, in the no-spoiler case, with respect to the applied refinement.

Case	Thrust (N)	Difference (%)	Number of cells (-)	Calculation time (h)
No refinement	66167.78	-2.24	28 M	40
Refinement 1	64848.53	0.2	43 M	60
Refinement 2	64783.68	0.1	117 M	100
Richardson extrapolation	64715.88	N/A	N/A	N/A

**TABLE 3** Comparison of the aerodynamic thrust, in the spoiler case, with respect to the applied refinement.

Case	Thrust (N)	Difference (%)	Number of cells (-)	Calculation time (h)
No refinement	66436.86	-1.53	29 M	40
Refinement 1	65417.63	0.03	45 M	60
Refinement 2	65427.46	0.02	115 M	120
Richardson extrapolation	65438.81	N/A	N/A	N/A

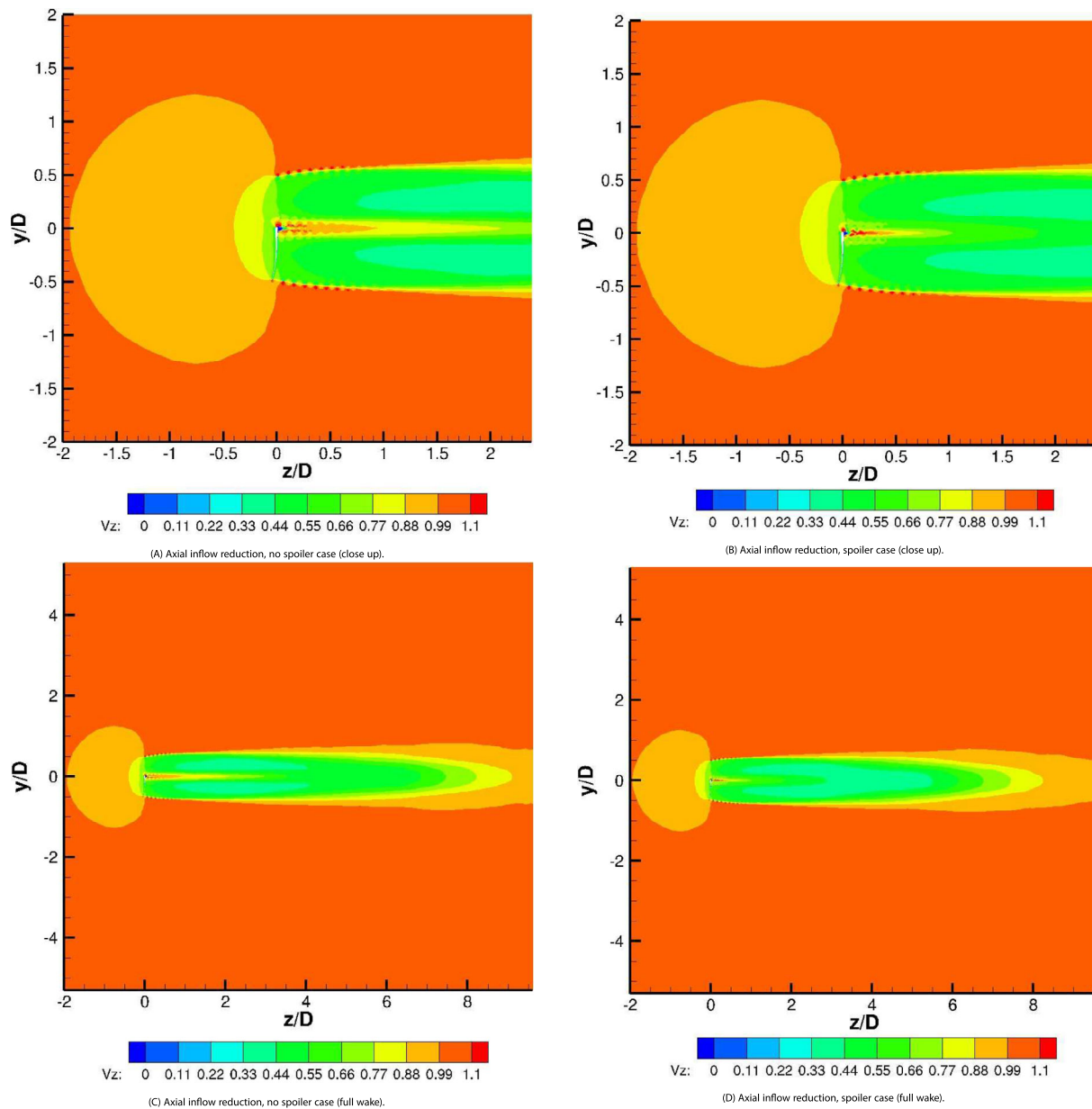


**FIGURE 4** Effect of the spoiler on the induction zone, near and far wake mixing. The inflow is dimensionless ( $V_z$ ) and flows from left to right.

induction extent can be highlighted using isocontour of the streamwise velocity in the  $Z - Y$  plane (see Figure 4). It clearly shows, for the spoiler and the no-spoiler case, that the induction area extends  $2D$  upstream of the rotor plane, with  $D$  the rotor diameter. Also this induction zone progressively decreases, for both cases, from  $Y/D = 0$  to  $Y/D \approx 1.25$  (light orange and yellow zone ahead of the rotor plane). In the defined induction area, the mean streamwise velocity reduces by up to 20%. All these observations are in good agreement with both the experimental<sup>19</sup> and the numerical literature<sup>20,21</sup> without spoiler. Since the induction area is identical in both cases, it indicates that, as expected, the spoiler has no effect on this area.

Behind the rotor, a near wake organization develops in two main areas: A centred cone area, starting at  $Z/D = 0$  and ending at  $Z/D = 3$ , in the no-spoiler case (see Figure 4A). Outside of the cone area, there exists a constant velocity deficit bounded by the well-known tip vortices (see the wavy surfaces of Figure 5A or the Q-criteria iso-contour of Figure 5B). This global organization found with and without spoiler agrees well with the existing literature.<sup>22</sup> In the presence of the spoiler, the cone size is largely decreased from more than  $3D$  diameters down to less than  $1D$  (estimated at the threshold level  $V_z = 0.66$  of the dimensionless streamwise velocity from Figure 4B). This is expected as the spoiler improves the blade root energy extraction and increases the flow mixing, thus reducing further the wind velocity in the near wake. Consequently, it increases the root loads, in good agreement with the flow reorganization observed in 2D simulations.<sup>8</sup> A slight overspeed is also noted for the root spoiler case, which might be attributed to the flow circumvention at the spoiler location. However, this local organization would certainly be highly influenced by the presence of the nacelle and would need further dedicated investigations.

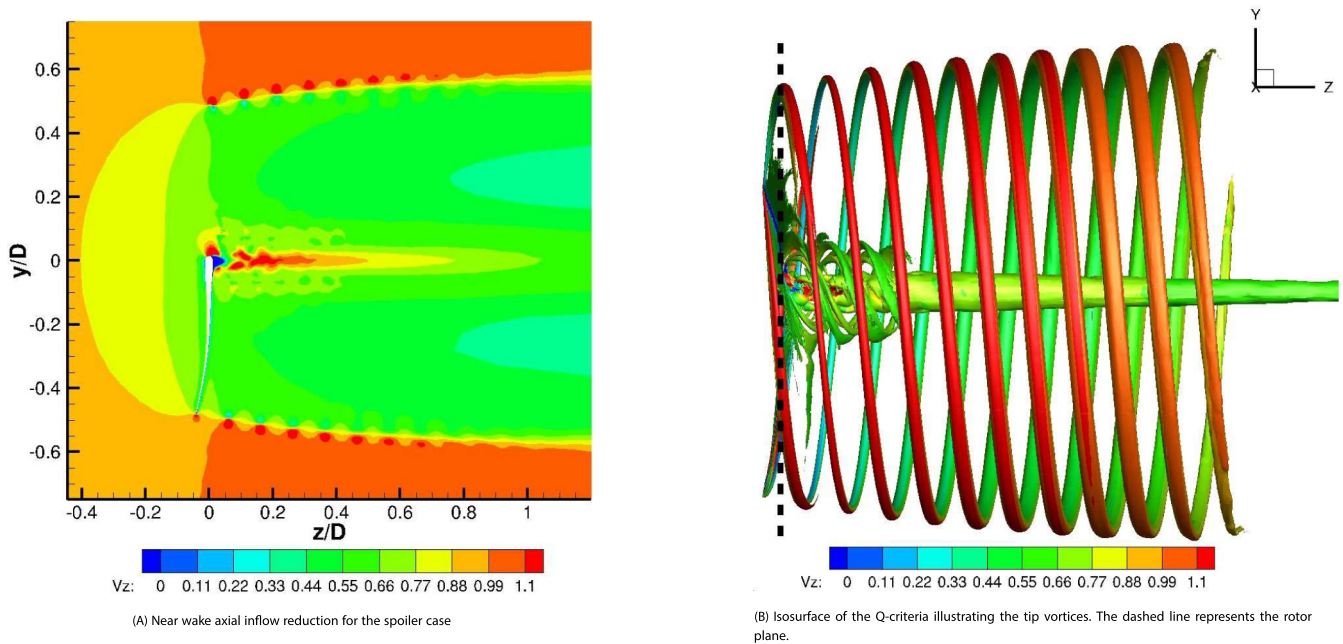


**FIGURE 5** Near wake description of the spoiler case.

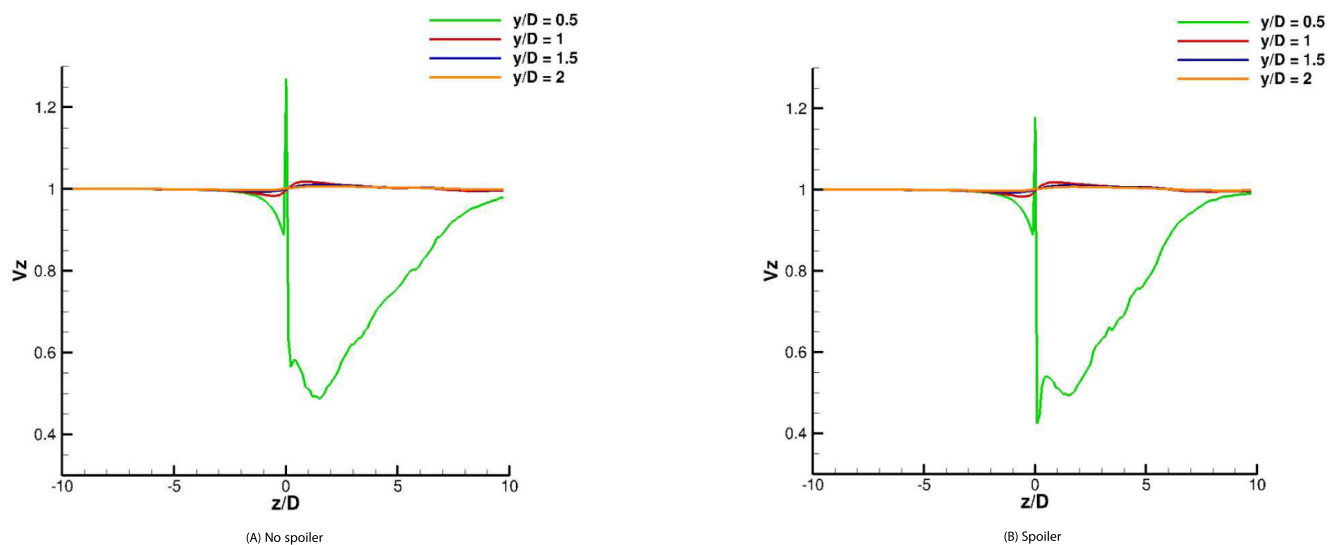


**FIGURE 6** Axial dimensionless velocity deficit at different rotor spanwise positions for the no spoiler and spoiler case.

Further along the blade span, the near wake deficit for the no-spoiler case is as important as in the spoiler case (approximately 60% of the inflow), meaning that blades are working efficiently to extract kinetic energy from the wind with or without spoiler. In the far wake, the recovery distance (taken at 99% of the streamwise velocity) without spoiler is around  $z/D=9$ , while it is  $8.5D$  for the spoiler case (see green lines on Figure 6A,B). This impact is four times smaller than the one observed in the near wake (cone reduction from  $3D$  to  $1D$ ). These results are showing similar tendency as what is generally underlined in the literature about the independence of the blade aerodynamic with the far wake.<sup>23,24</sup>

## 4.2 | In the rotor plane

After investigating upstream and downstream the rotor, the following sections will focus on the rotor plane region with observations of the spoiler impact on the local axial and tangential inductions and on the local angle of attack.

### 4.2.1 | Axial induction

Following the classical BEM theory,<sup>25,26</sup> the axial induction is defined as:  $a = 1 - \frac{U_z}{V_0}$ , where  $U_z$  is the velocity in the z-direction and  $V_0$  is the free-stream velocity. The axial induction evolution along the blade radius shows its efficiency to extract energy (see Figure 7B). According to the BEM theory, the optimal induction along the blade radius is  $a = 1/3$ . The extraction of the blade related velocities using the AAT method<sup>27,28</sup> can be used to obtain the inductions in the rotor plane.

Figure 7A shows the axial induction in the rotor plane for the spoiler case. It clearly highlights that the highest energy extraction is located in midspan and outer part of the blade. The energy extraction at the root and tip area is degraded due to respectively the tip vortices and the 3D flow organization at the root, as previously described.<sup>29</sup> The spoiler effect is seen on the blade inboard on Figure 7B: The induction increases significantly where the spoiler is installed, from  $0.03 < r/R < 0.17$ , marked by a grey shaded area. The end of the spoiler is marked by a drop in induction before an increase where the blade becomes more aerodynamic.

### 4.2.2 | Tangential induction

Regarding the tangential induction, it can be obtained from the ratio between the local tangential flow velocity and the local rotational speed, that is,  $a' = -U_x/\omega r$ , where  $U_x$  is the induced tangential flow velocity,  $\omega$  the blade rotational speed, and  $r$  the considered radius.<sup>30</sup> Figure 8A shows its evolution along the blade radius without and with the spoiler. Similarly to the axial induction, the tangential induction is significantly increased at the blade root with a spoiler. This increase is linked to the extent of the cone area behind the rotor detailed in Section 4.1.

At this stage, it is interesting to evaluate the angle of attack modification from these two induction quantities.

### 4.2.3 | Angle of attack

The relationship between the inductions and the angle of attack translates into:  $\alpha = \varphi - \theta$  where  $\varphi$  is the inflow angle and  $\theta$  is the sum of the blade pitch and local twist. The inflow angle is calculated using the axial and tangential induction:  $\varphi = \arctan \frac{U_x(1-a)}{\omega r(a+1)}$ . Figure 8B shows the computation of the angle of attack evolution along the blade radius without and with spoiler using previous axial and tangential inductions. As expected, the blade inboard experiences high angles of attack without spoiler where the local section operates in the stall region. The spoiler tends to reduce the local operating angle of attack where installed, although the section still operates in the stall region. This is mostly due to the axial induction increase and partly thanks to the tangential induction increase. Lowering the angle of attack would mean that the local sections will operate at

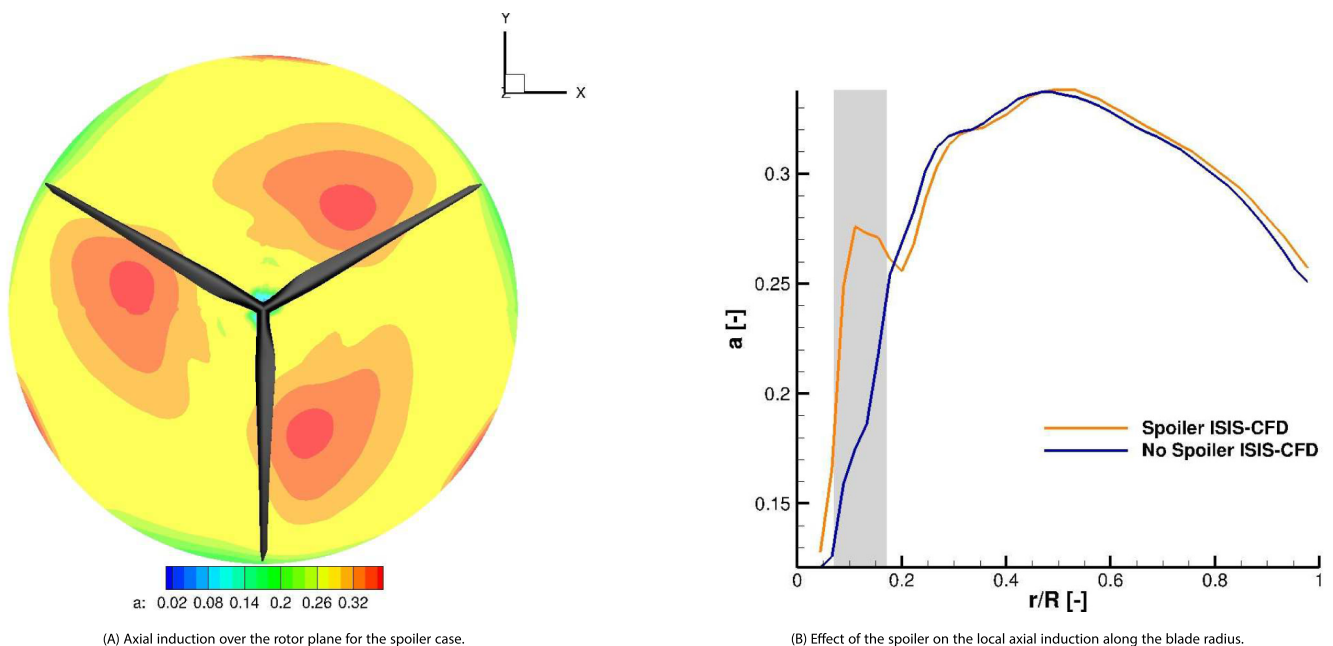
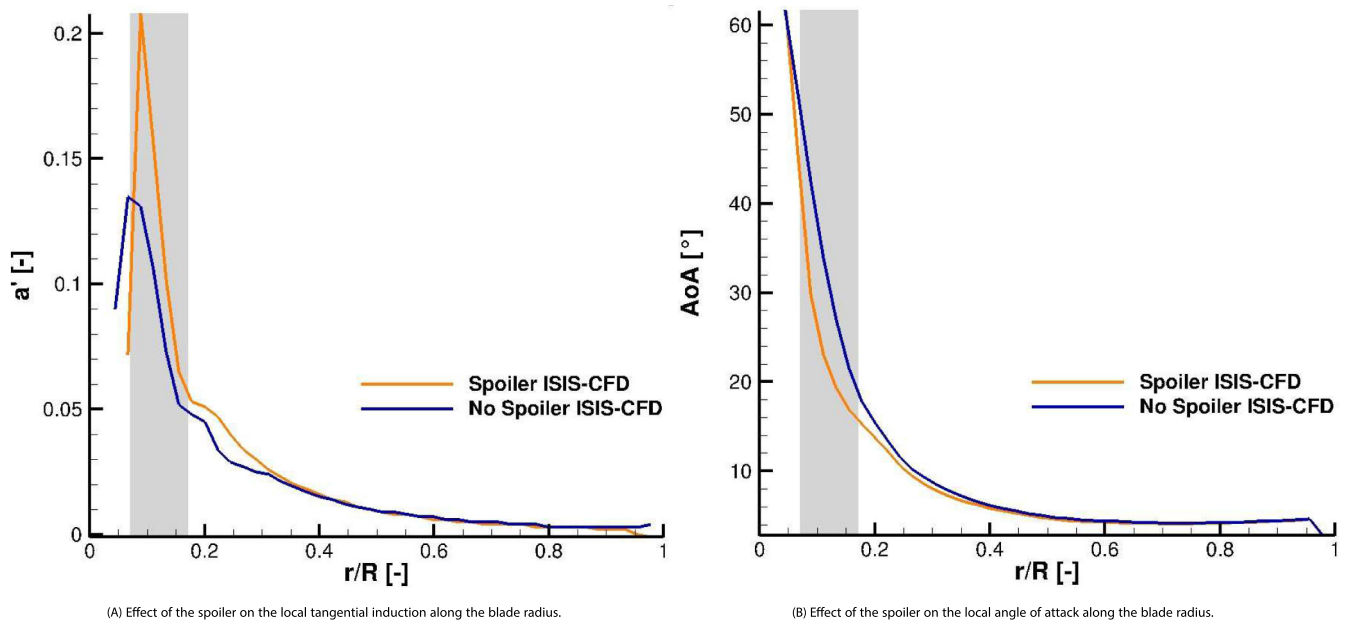


FIGURE 7 Axial induction in the rotor plan and radial evolution.



**FIGURE 8** Tangential induction and angle of attack evolution for both no spoiler and spoiler case.

lower  $C_L$  and  $C_D$ . It will also operate closer to the linear region, thereby limiting the harmful effects of the stall region. However, as it is shown in the following sections, the spoiler effect is not strong enough to remove the flow separation region.

## 5 | AT THE BLADE SCALE

This section aims at understanding the spoiler impact at blade level. Locating first the modified area, the flow reorganization is then described. Impact on local loads is presented and the description of the blade wake dynamics reorganization follows.

The coordinate system used in the following is attached to the blade, with its centre at the intersection of the three blade axis. The x-axis is along chordwise direction, the y-axis is along the blade length and the z-axis is orthonormal to the x-axis and y-axis.

### 5.1 | Identification of the impacted area

The 3D flow organization at the root area is first analysed in this section through the mean wall shear stress (WSS) quantity in the chordwise direction,  $\tau_x$ , and in the spanwise direction,  $\tau_y$ , to have a global overview of the impacted area by the spoiler. It is defined by the following equations and its unit is in  $[N/m^2]$ :

$$\tau_x = \mu \left( \frac{\partial U_x}{\partial z} \right) \Big|_{z=0} \quad \tau_y = \mu \left( \frac{\partial U_y}{\partial z} \right) \Big|_{z=0} \quad (1)$$

$U_x$  is the x-axis velocity component,  $U_y$  is the y-axis velocity component,  $z$  the direction normal to the rotor surface, and  $\mu$  is the dynamic viscosity.

Wall shear stress isocontours for the two directions are plotted on the inboard region of the blade in Figure 9A,B for the no spoiler and the spoiler cases.  $\tau_x$  shows a clear region where its value is negative (in cyan), indicating a reverse flow region of the  $U_x$  component. This region extends until  $r/R \approx 20\%$  in both cases in good agreement with the literature.<sup>31,32</sup> This region is bounded by transitional regions where the WSS is no longer negative but still lower than the rest of the blade (in yellow). The spoiler does not remove the reverse flow region; on the contrary, it increases slightly.

On the other hand, the wall shear stress value component along the blade length,  $\tau_y$ , in Figure 9B underlines a region in red, until  $r/R \approx 0.3$ , where the WSS is positive. This region remains almost unchanged when a spoiler is installed and is related to the well-known crossflow due to the rotation as described in Section 6.

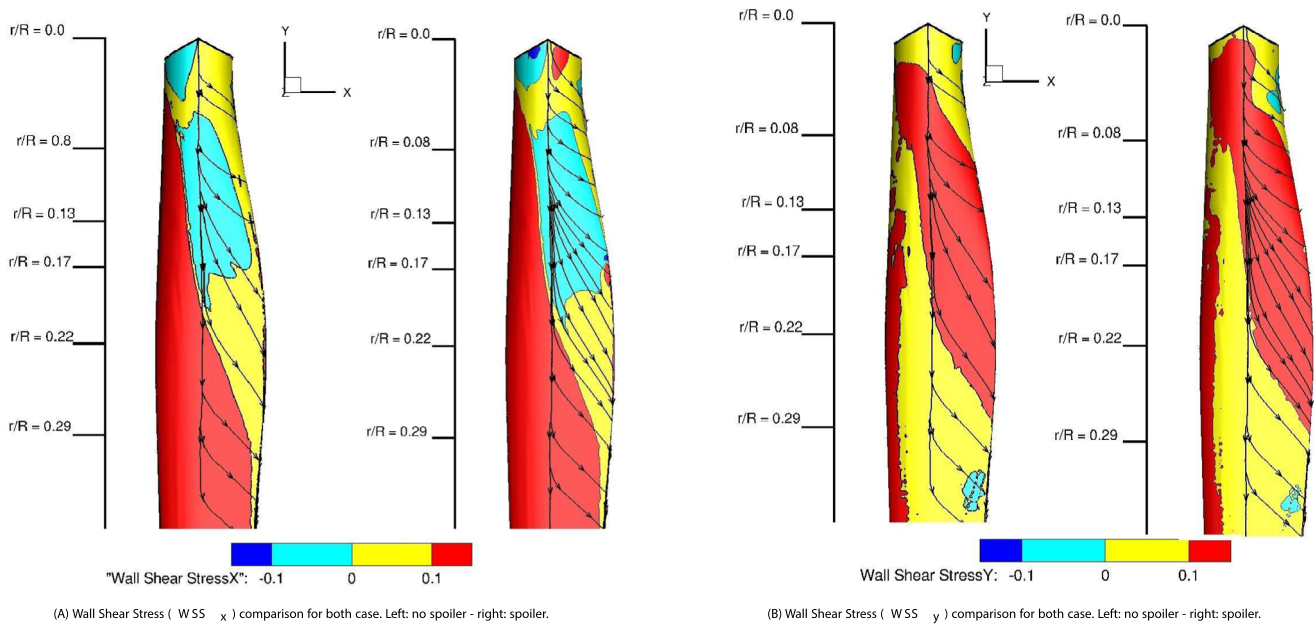


**FIGURE 9** Wall shear stress comparison for both case in the following the x and y directions.

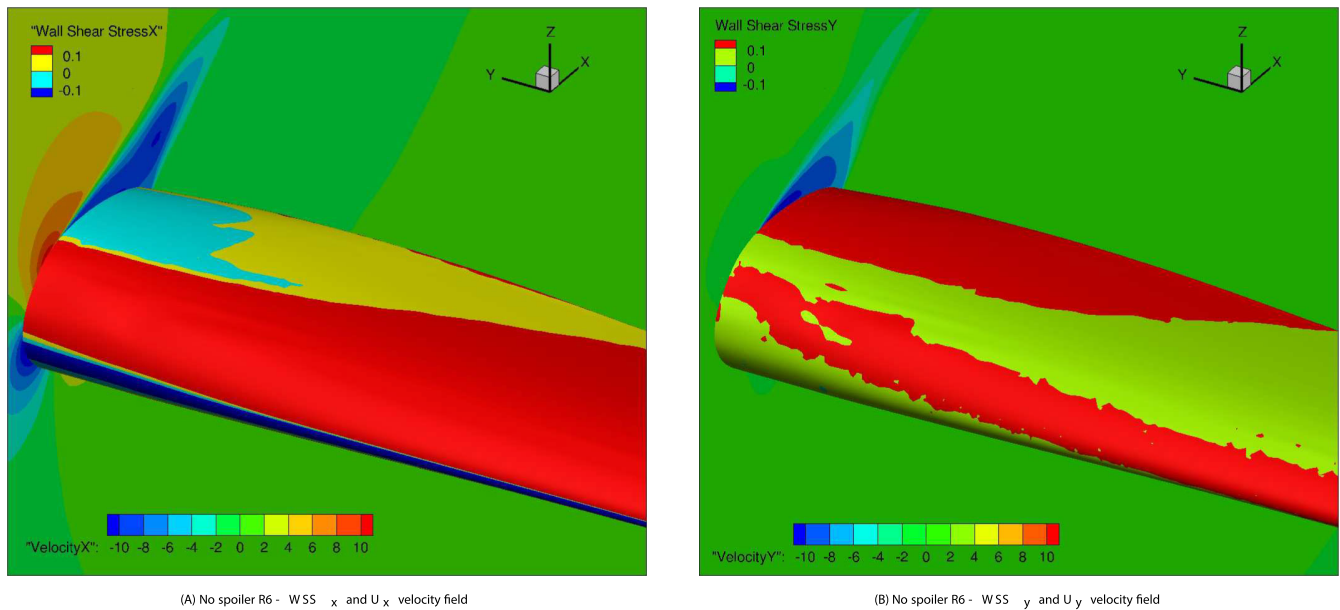


**FIGURE 10** Wall shear stress and velocity field for the no-spoiler cases following the x-axis and y-axis. Respectively the chordwise and spanwise direction. The velocity field intersects the blade at  $r/R = 0.13$ , the blade can be seen up to  $r/R = 0.4$

It should be noted that both WSS components are calculated using URANS simulations and exhibit a beating movement in the radial direction that will be discussed further in the unsteady investigation of Section 6.3. To understand in more details the wall shear stress distribution, it is analysed in the next section with respect to the velocity field organization.

## 5.2 | The blade root flow organization

Figures 10 and 11 show, respectively, isocontours of the velocity  $U_x$  and velocity  $U_y$  at the radial position  $r/R = 0.13$  in an isometric view, overlapped with the previously illustrated wall shear stress. The figures show the blade from  $r/R = 0.13$  to  $r/R = 0.4$ . Isocontour of the

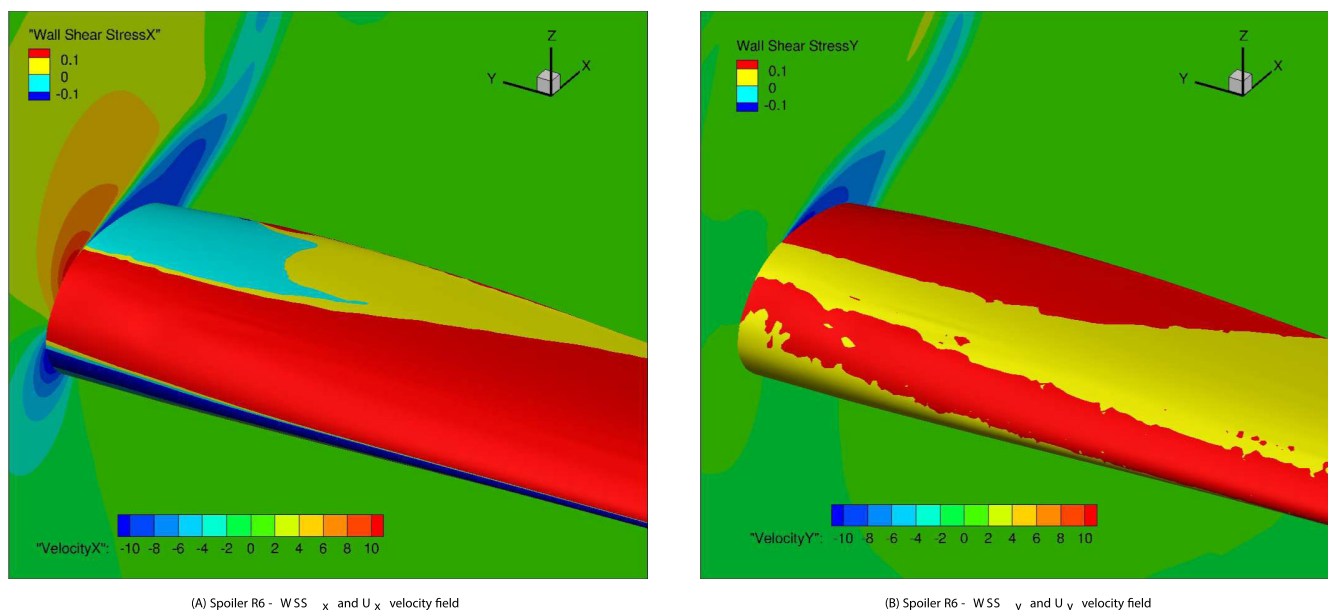


**FIGURE 11** Wall shear stress and velocity field for the spoiler cases following the x-axis and y-axis. Respectively the chordwise and spanwise direction. The velocity field intersects the blade at  $r/R = 0.13$ , the blade can be seen up to  $r/R = 0.4$

chordwise velocity ( $U_x$ ) clearly evidences the flow separation region in good agreement with the negative wall shear stress region shown in the previous section. Moreover, the other velocity component (the spanwise velocity  $U_y$ ), in Figure 10B highlights the Himmelskamp (or Coriolis) effect (also seen on Figure 9B). This last flow organization induces an increase of the wall shear stress spanwise component that is found responsible of a pressure increase on the blade suction side noticed in the following section (see Figure 19B). Indeed, the chordwise velocity component exhibits a flow separation and thus normally a zero pressure gradient evolution. This Coriolis beneficial effect is retrieved and described in the literature.<sup>29</sup> The spoiler does not impact significantly this phenomenon, the cross-flow region being only slightly increased (see Figure 11A), and the separated region is almost unchanged. Therefore, the previously observed impact of the spoiler in Section 4.1: The cone reduction, the angle of attack reduction, and the axial and tangential induction increase cannot be attributed to the improvement of the flow separation by the spoiler, nor the increase of the beneficial cross-flow effect. It should be rather linked to the spoiler ability to reorganize the pressure distribution around the aerofoil, which is investigated in the next section.

### 5.3 | Impact on blade loads

The following section will detail the spoiler impact on the mean local wall pressure coefficient ( $C_p$ ) and lift coefficient evolution in 3D for the radial position  $r/R = 0.13$ . In both spoiler and no-spoiler cases, the separated flow region does not exhibit a flat  $C_p$  distribution (zero pressure gradient) in the trailing edge region. This is to be attributed to the beneficial Coriolis effect described in the previous section. As a reminder, the spoiler is installed on the pressure (bottom) side of the aerofoil. When the spoiler is installed, the impact on the pressure is mostly found on the pressure side (bottom curve), with  $C_p$  being only slightly increased in the suction side. This induces an increase of the mean  $C_L$  value (see Figure 12B), and a decrease of the moment coefficient as the aerofoil loading is more evenly distributed rather than front loaded (not shown here). The lift is not steady due to two phenomena observed in simulations (see short movies available online<sup>33,34</sup>): Vortex shedding from the unsteady blade wake organization and transverse flow unsteadiness. The spoiler increases significantly these lift oscillations, similarly to the findings in 2D simulations.<sup>8</sup> The following section will examine in more detail this unsteady organization.

### 5.4 | Unsteady investigation

The following section will first investigate the possible sources of unsteadiness responsible of the lift fluctuations. In the following, the focus will be on the radial location  $r/R = 0.13$ .

The main known source of unsteadiness is the vortex shedding from the blade wake organization. Figure 13 shows for both cases, no spoiler and spoiler, the 3D simulations outcome of the vorticity and Q-criteria. The Q-criteria is illustrated by black lines following a logarithmic increment

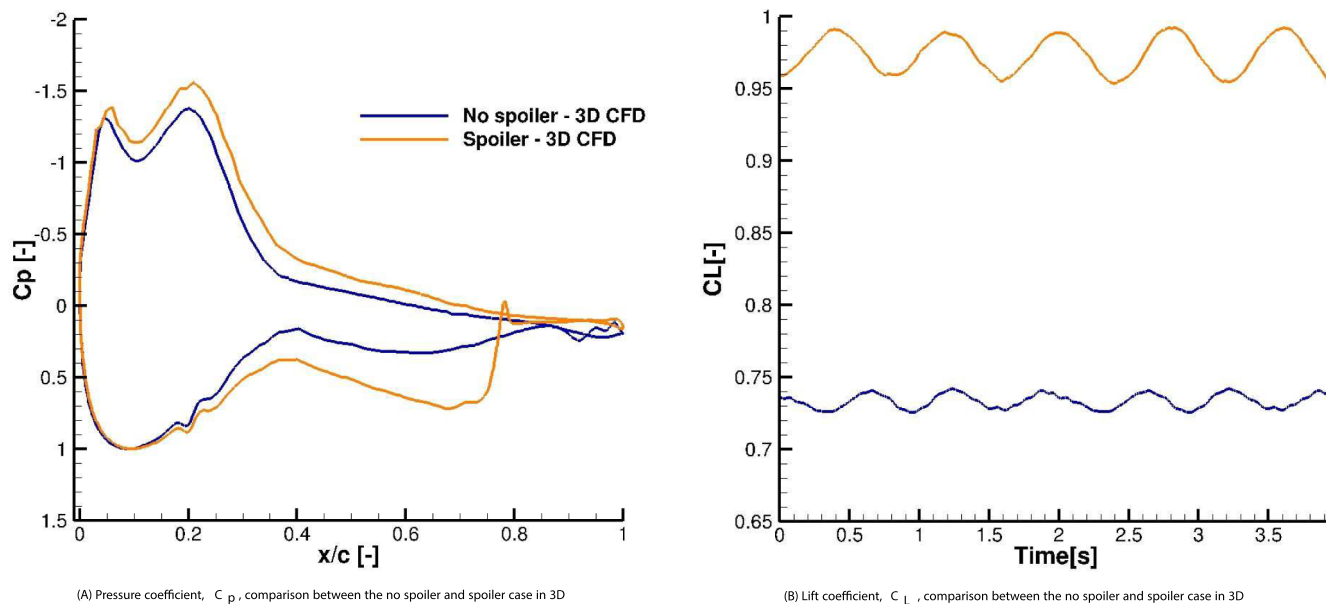


FIGURE 12 Comparison of the  $C_p$  and  $C_L$  in 3D for the no spoiler and spoiler case.

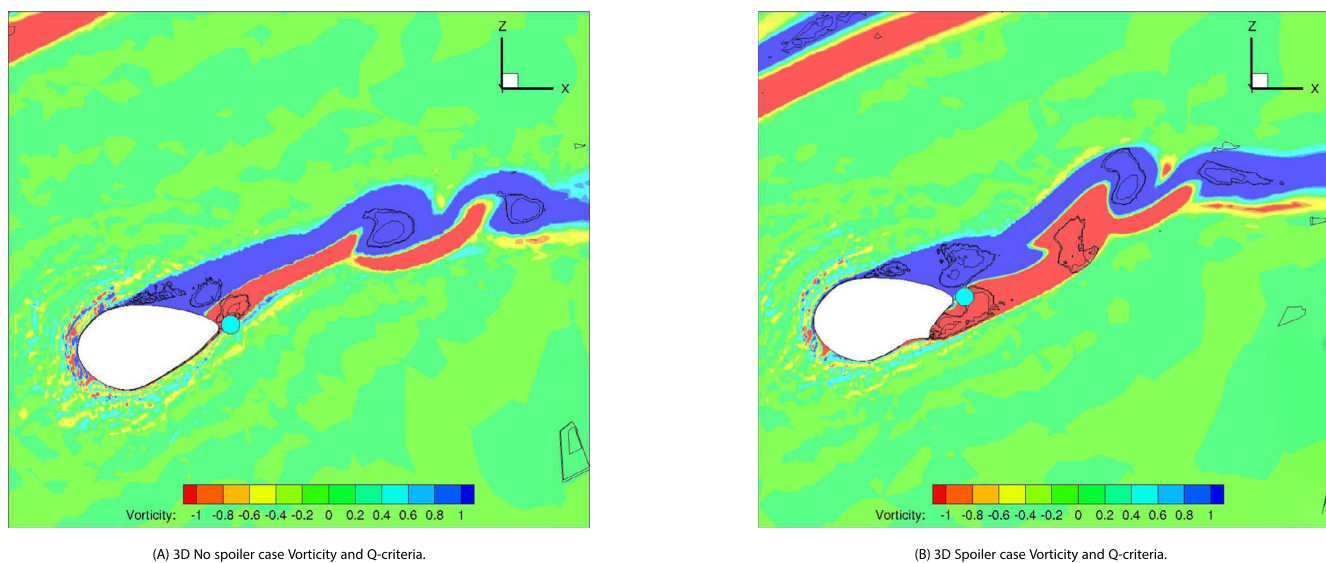
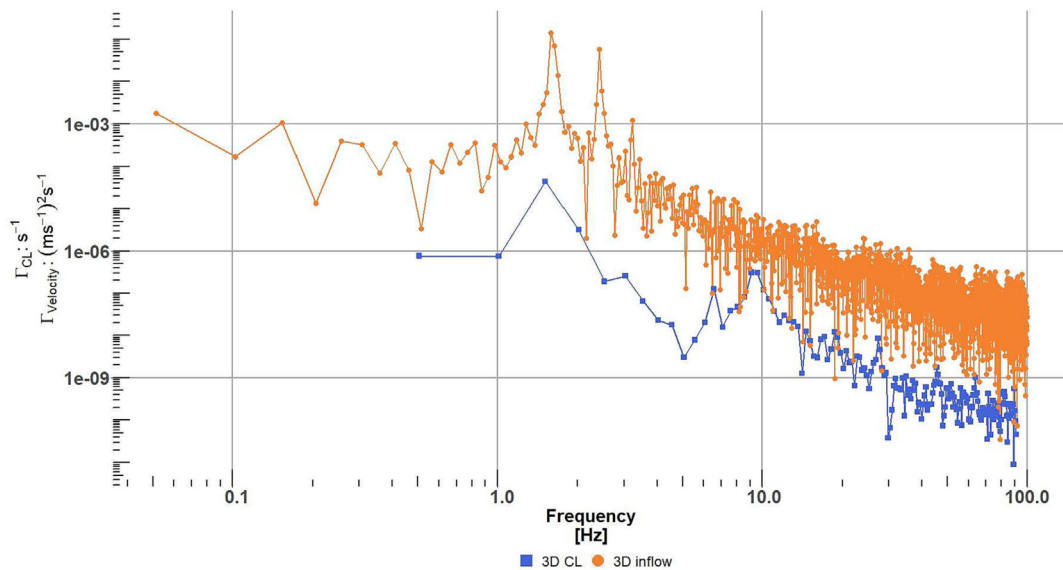


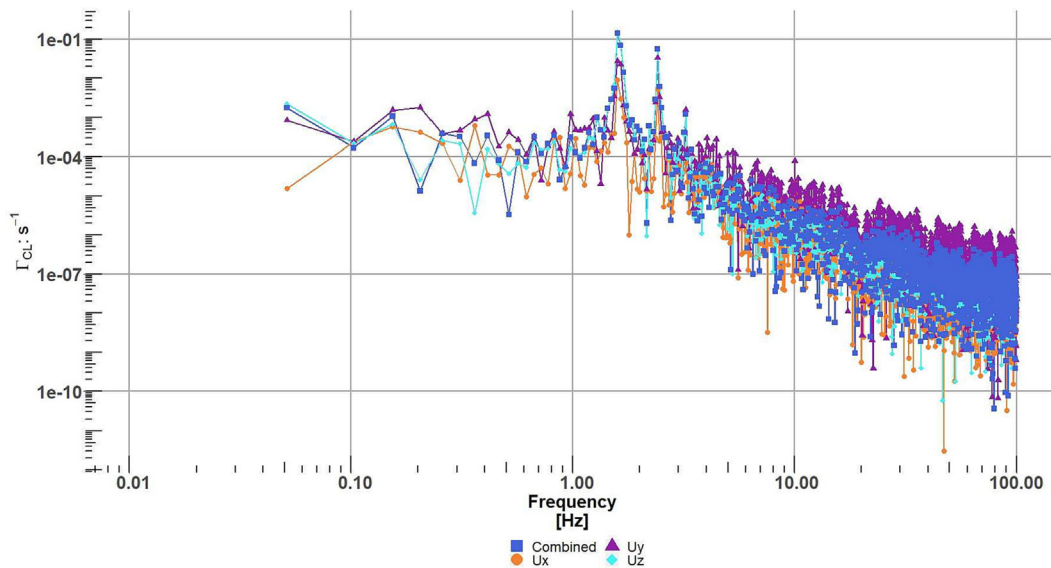
FIGURE 13 No spoiler and spoiler case 3D vorticity and Q-criteria, operating following the conditions of Table 4. The probing point is shown as the cyan dot (●) near the aerofoil's trailing edge.

TABLE 4 Three-dimensional operational conditions for the no spoiler and spoiler at the radial position  $r/R = 0.13$ .

Conditions	No spoiler	Spoiler
Rotation speed	14.1 RPM	
Relative velocity	11.5 m/s	11.4 m/s
Angle of attack	27°	19.3°
Reynolds number	$2.42 \times 10^6$	$2.39 \times 10^6$
Chord	3.1 m	



**FIGURE 14**  $C_L$  and relative velocity power spectral density of the no-spoiler case in 3D. The blue square (■) shows the 3D  $C_L$  results and the orange dot (●) shows the 3D relative velocity results.



**FIGURE 15** Comparison of the power spectral density for the relative velocity and its components in the three dimensions for the no-spoiler case. The blue square (■) shows the relative velocity, the orange dot (●) shows x-axis velocity component, the purple triangle (▲) shows y-axis velocity component and the cyan diamond (◆) shows z-axis velocity component.

between 0.1 and 1000. Due to the blade rotation, the vortices are elongated and no longer circular as described later in Section 6.2 in more details. They are however present and tend to move “upward,” following the main inflow direction. This behaviour is thus creating the cone noticed near the centre of rotation in Figure 5B.

The spoiler case exhibits a wider wake than the no-spoiler case, similar to previous 2D simulations.<sup>8</sup> The vortex shedding organization seems to be also impacted. In the following plots (Figures 14–17), a spectral analysis is performed in the wake region from a probing point located after the trailing edge. It is located 10% of the local chord after the trailing edge and aligned with the blade’s section chord (see Figure 13). It is compared with the spectral analysis of the lift fluctuation at this section, for the no spoiler and spoiler cases. In the following figures, “3D CL” refers to the lift coefficient calculated by integrating the pressure coefficient around the aerofoil from 3D CFD simulations. “3D Inflow” refers to the measured data through a probing point positioned in the wake of the 3D blade.

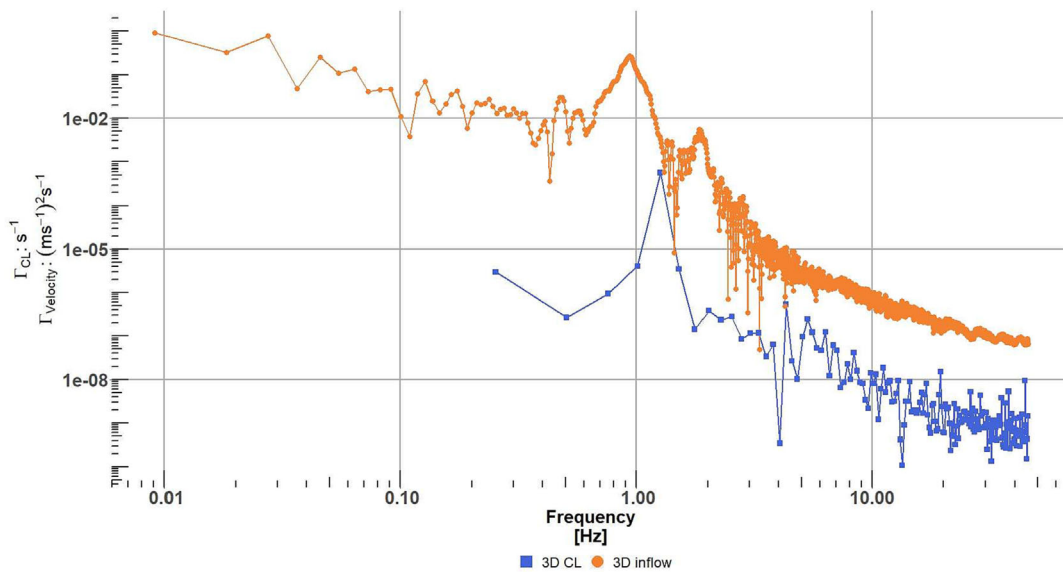


**FIGURE 16**  $C_L$  and relative velocity power spectral density of the spoiler case in 3D. The blue square (■) shows the 3D  $C_L$  results and the orange dot (●) shows the 3D relative velocity results.

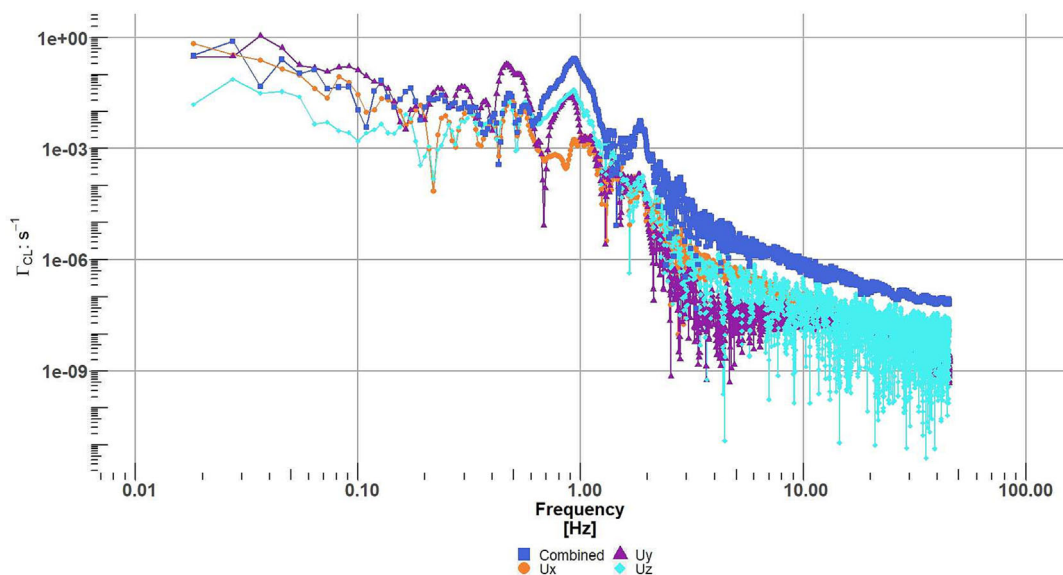


**FIGURE 17** Comparison of the power spectral density for the relative velocity and its components in the three dimensions for the spoiler case. The blue square (■) shows the relative velocity, the orange dot (●) shows x-axis velocity component, the purple triangle (▲) shows y-axis velocity component, and the cyan diamond (◆) shows z-axis velocity component.

The no-spoiler case shows that both main peak frequencies from the sample signal in the aerofoil's wake and from the lift signal happen around 1.5 Hz (see Figure 14). The  $C_L$  power spectral density (PSD) fails to capture the first harmonic seen in the wake velocity signal. Although the aerofoil is 60% thick, this behaviour falls in line with the well-known cylinder behaviour:  $C_L$  carries the main frequency while  $C_D$  carries the first harmonics and is always twice as high as the peak frequency.<sup>35</sup> In the wake, both information are available through the air velocity and therefore the main frequency and harmonics are seen.

Aside from the main inflow direction ( $U_z$ ), the main component of the peak frequency is  $U_y$ . It corresponds to the cross-flow pulsing from the blade root towards the tip as clearly seen on Figure 15. The blue square (●) on Figures 15 and 17 corresponds to the vectorial sum of  $U_x$ ,  $U_y$ , and  $U_z$ , that is, the velocity vector  $\mathbf{U}$ .

In the spoiler case, the peak frequency measured in the wake of the aerofoil is much broader than the one from the lift coefficient and occurs at a slightly lower frequency level,  $\approx 1$  Hz (see Figure 16). The wake being broader in the spoiler case, the associated vortices are larger. It induces

a slower convective velocity of these vortices and thus a lower shedding frequency. The broader peak frequency can be explained by either a merging of vortices or the perceived area by the flow is “less smooth” due to the spoiler’s presence. However, the most probable scenarios are either a different contribution from other velocity components or because the probe in the wake is capturing trailing flow from previous radial positions as illustrated by the inclined streamlines on Figure 9A. Indeed, no vortex merging were observed and the vortices do not leave the trailing edge in a similar fashion. As shown in Figure 13, for the no-spoiler case, the probing point is at the edge of the wake, while in the spoiler case, it is in the middle of the bottom vortex.

Similar to the no-spoiler case,  $U_z$  and  $U_y$  are the main contributors of the peak frequency. Dedicated studies to discriminate the influence of the rotation and the blade span would be necessary to identify the independent effects on the spectral broadening.

The main difference between choosing the wake velocity or the  $C_L$  for performing a PSD analysis is the energy within the spectrum. The energy contained in the lift spectrum is much lower than the energy captured in the relative velocity as indicated by the difference in the levels of the power spectrum in Figures 14 and 16. Otherwise the predicted vortex shedding frequency (VSF) in both methods is quite similar. Because the ultimate goal is its use in fatigue analysis, the case without and with the spoiler are compared using loads, here the sectional  $C_L$ , in Figure 18. It shows that, in 3D, the addition of the spoiler to a blade section does not change significantly the VSF, despite the different angle of attacks. Indeed both peak frequencies are close to each others ( $f_1 = 1.26$  Hz and  $f_2 = 1.52$  Hz). Two main contradicting effects can explain the differences in VSF: The change in angle of attack and the wake widening due to the spoiler addition. The spoiler reduces the local angle of attack, which tends to increase the VSF. However, the spoiler’s other characteristics is that it widens the wake behind the aerofoil, which tends to reduce the VSF. Figure 18 indicates that the wake widening effect is stronger than the angle of attack reduction.

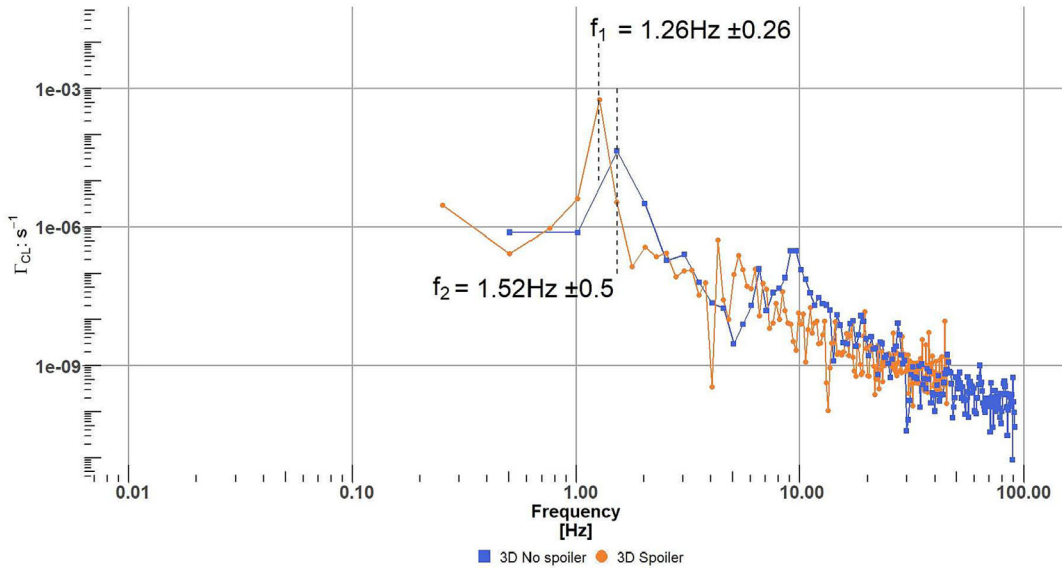


**FIGURE 18**  $C_L$  power spectral density for both cases in 3D. The blue square (■) shows the  $C_L$  results for the no-spoiler case in 3D and the orange dot (●) shows the  $C_L$  results for the spoiler case in 3D. The “±” symbol corresponds to the spectral discretization used.

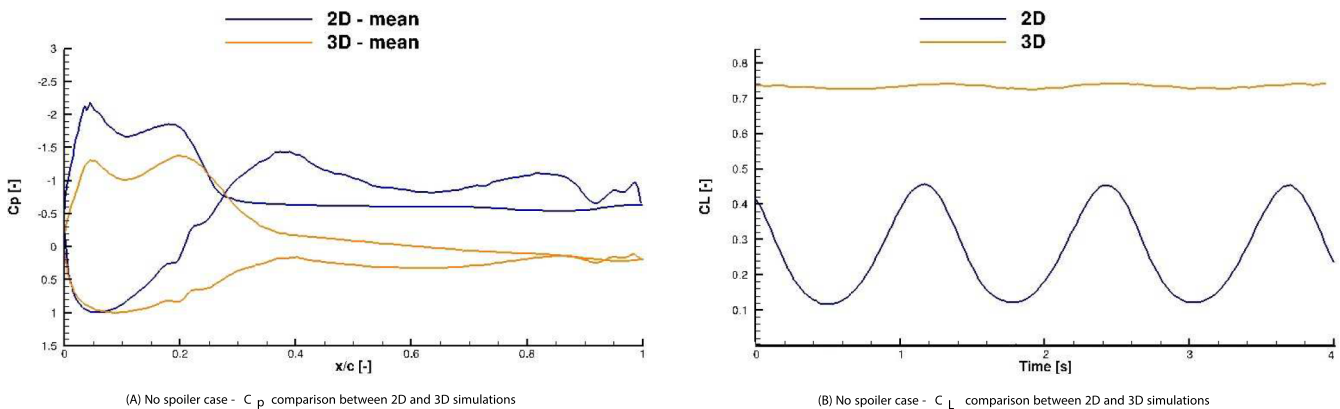


**FIGURE 19** Comparison of the wall pressure coefficient,  $C_p$ , (left) and the lift coefficient  $C_L$ , (right) for the no-spoiler case, in 2D and 3D.

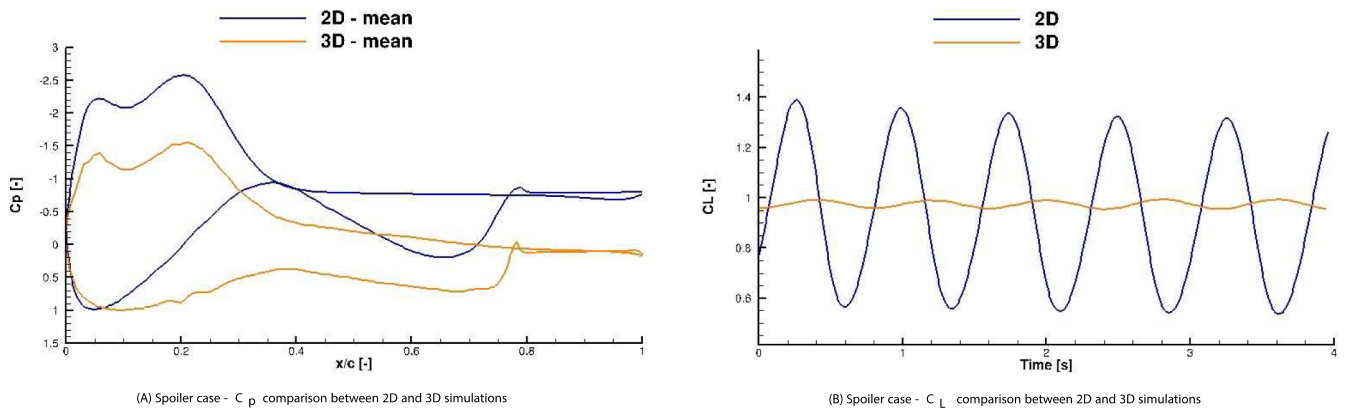


**FIGURE 20** Comparison of the wall pressure coefficient,  $C_p$ , (left) and the lift coefficient  $C_L$ , (right) for the spoiler case, in 2D and 3D.

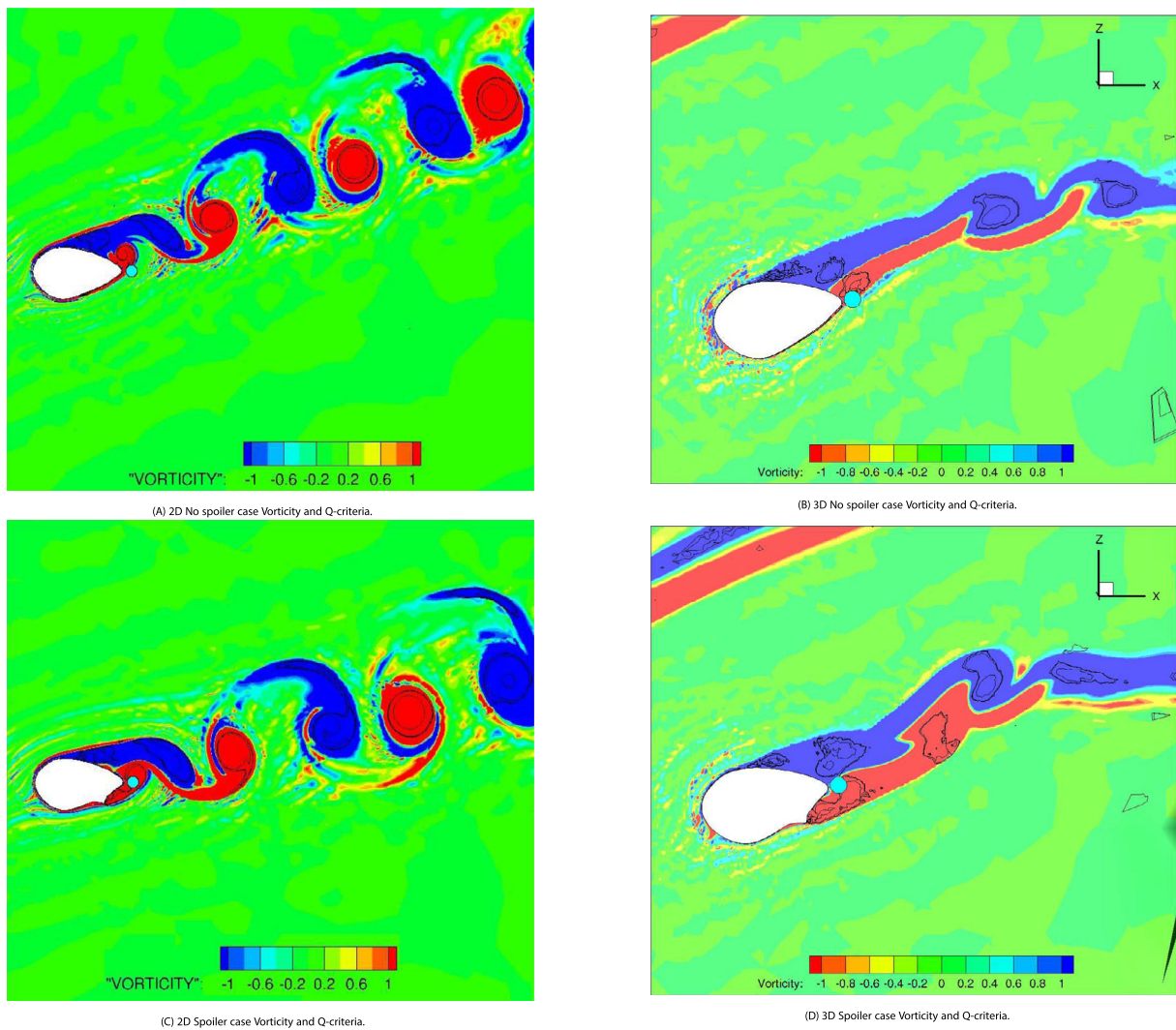


**FIGURE 21** No spoiler and spoiler case vorticity and Q-criteria comparison between 2D and 3D, operating following the conditions of Table 4. The probing point is shown as the cyan dot near the aerofoil's trailing edge.

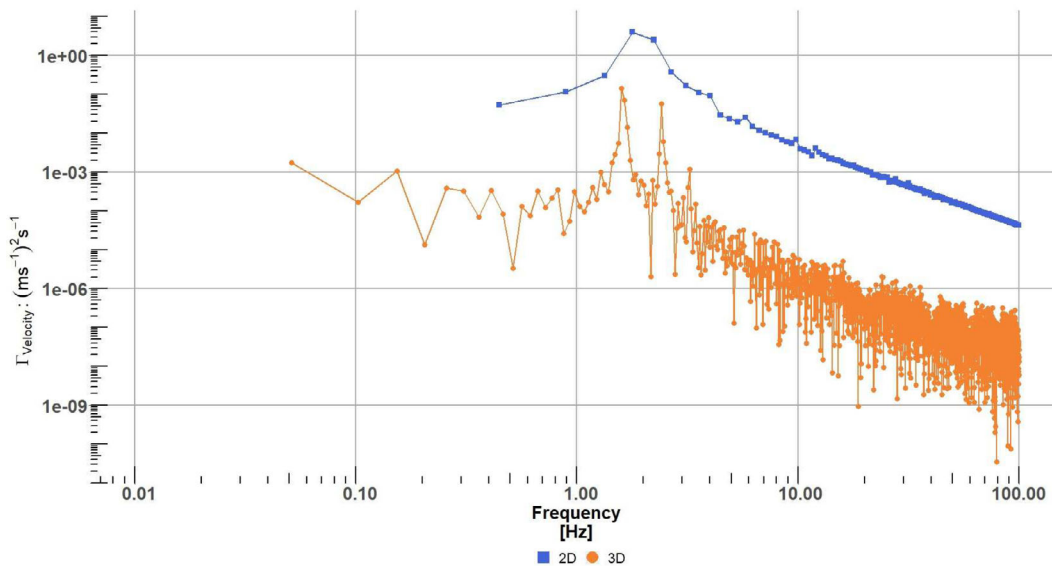
## 6 | AT AEROFOIL SCALE

Increasing simulation fidelity increases the computational time. The impact of fidelity simulations on the spoiler effect is evaluated here. The difference in simulation fidelity is first presented at the aerofoil scale by comparing 2D URANS simulations with aerofoil cross sections of 3D URANS simulations. The comparison will be presented at the radial position  $r/R = 0.13$

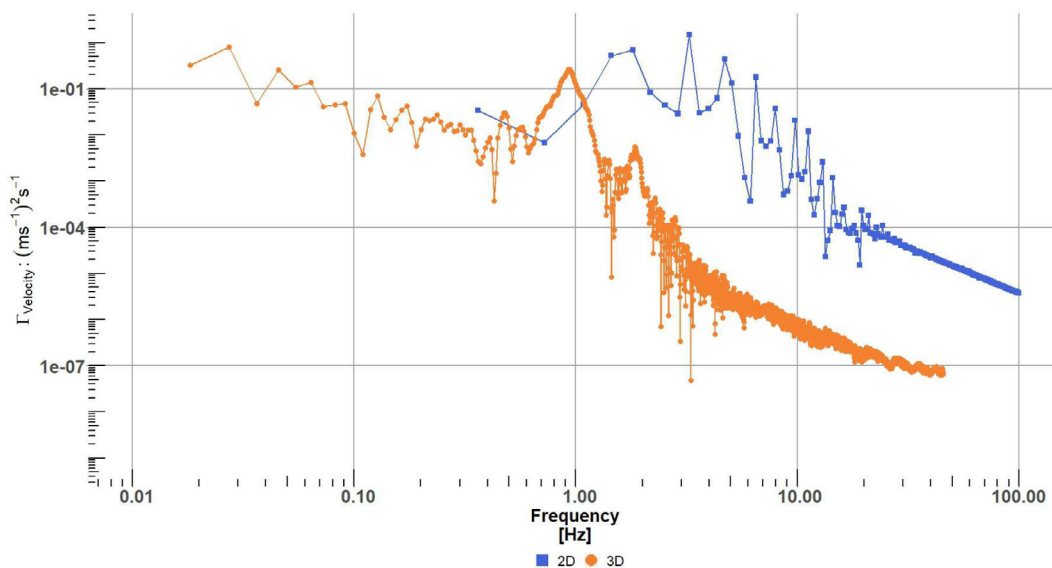
Finally 3D URANS simulations are briefly compared with DDES simulations.

### 6.1 | Aerofoil local and global loads

The wall pressure coefficient,  $C_p$ , is used to help define the possible separation along the aerofoil. Flow separation occurs after a sharp adverse pressure gradient and can be observed on a  $C_p$  plot in the region exhibiting a plateau. Such example occurs at  $x/c = 0.25$  on Figure 19B for the



(A) Relative velocity Power Spectral Density of the no spoiler case in 2D and 3D.



(B) Relative velocity Power Spectral Density of the spoiler case in 2D and 3D.

**FIGURE 22** Relative velocity power spectral density of the no spoiler and spoiler case in 2D and 3D. The blue square (■) shows the 2D relative velocity results and the orange dot (●) shows the 3D relative velocity results.

2D case while it is not present in 3D simulations, for both cases (without and with spoiler). Also, integrating the area comprised between the two  $C_p$  curve (suction side and pressure side) allows for the calculation of the local lift coefficient  $C_L$  and drag coefficient  $C_D$ . The velocities used to calculate the different metrics have been extracted using the AAT method.<sup>27,28</sup>

Figures 19 and 20 show the differences at aerofoil level between 2D and 3D CFD simulations through the comparison of the mean local wall pressure coefficient,  $C_p$ , and the instantaneous lift coefficient,  $C_L$ . For both cases, the no spoiler and the spoiler case, the pressure coefficient distribution exhibits a plateau and thus a separated flow area in 2D that is not present in 3D simulations. It is due to the cross-flow and the Coriolis effect in good agreement with the stall delay phenomenon found in the literature<sup>36,37</sup> and already discussed in Section 5. For the no-spoiler case, the impact of the mean lift level due to this Coriolis effect is found to be almost tripled, from  $C_L^{2D} \approx 0.25$  to  $C_L^{3D} \approx 0.75$  (see Figure 19B).

The difference between the 2D and 3D simulations in terms of mean lift coefficient is less important for the spoiler case,  $C_L^{2D} \approx 0.92$  and  $C_L^{3D} \approx 0.97$  (see Figure 20B). It is to be noticed that even if the mean lift value is similar, there is a significant difference in the pressure distribution, that is more balanced in the chordwise direction in 3D than in 2D simulations. The results also show that 3D simulations significantly dampen the

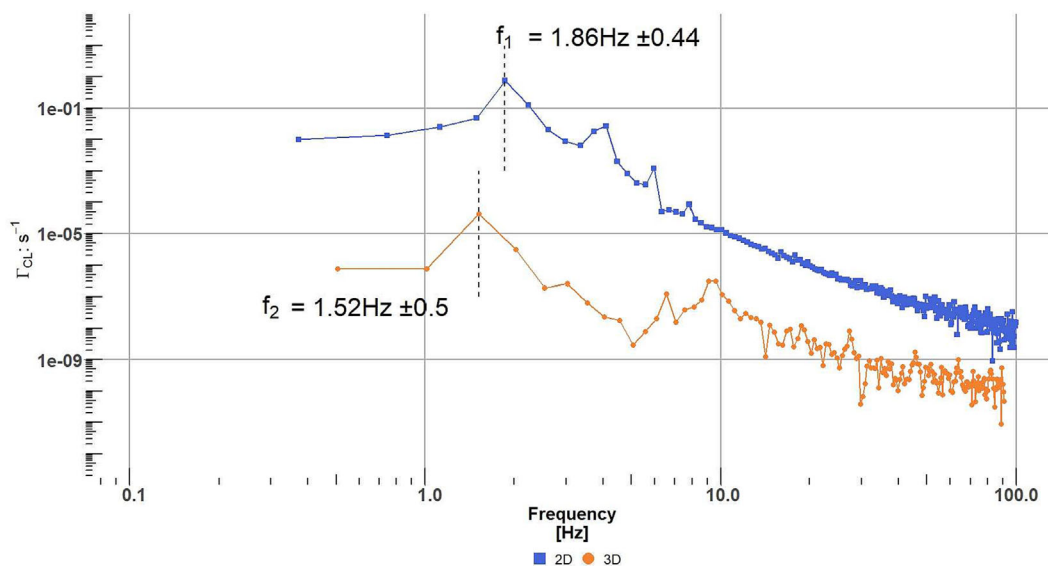


**FIGURE 23** No spoiler power spectral density comparison of the  $C_L$ . The blue square (■) shows the 2D  $C_L$  results and the orange dot (●) shows the 3D  $C_L$  results. The “±” symbol corresponds to the spectral discretization used.

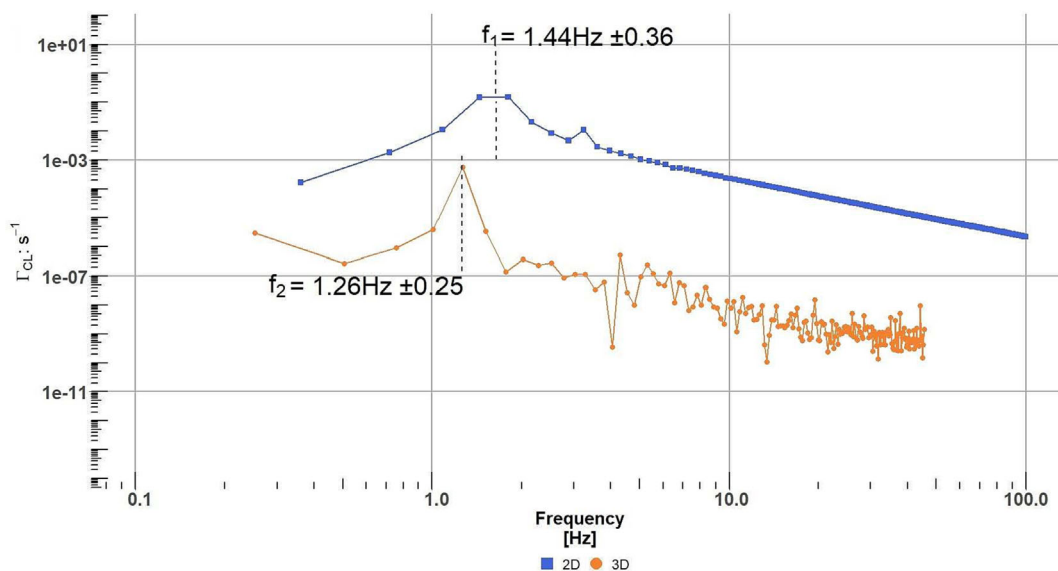


**FIGURE 24** Spoiler power spectral density comparison of the  $C_L$ . The blue square (■) shows the 2D  $C_L$  results and the orange dot (●) shows the 3D  $C_L$  results. The “±” symbol corresponds to the spectral discretization used.

amplitude of oscillations in both spoiler and no-spoiler case (Figures 19B and 20B). To understand further, the unsteady aerofoil wake organization is analysed in the following section.

## 6.2 | Aerofoil unsteady wake investigation

The following section will verify the validity of the assumption that the VSF is affected neither by the blade's span nor its rotation and that 2D simulations can, in a first design approach for fatigue calculation, represent the unsteady behaviour of the flow past the aerofoil. Figure 21 highlights differences between 2D and 3D simulations on the aerofoil wake flow organization. Globally, with or without spoiler, vortices in the 2D

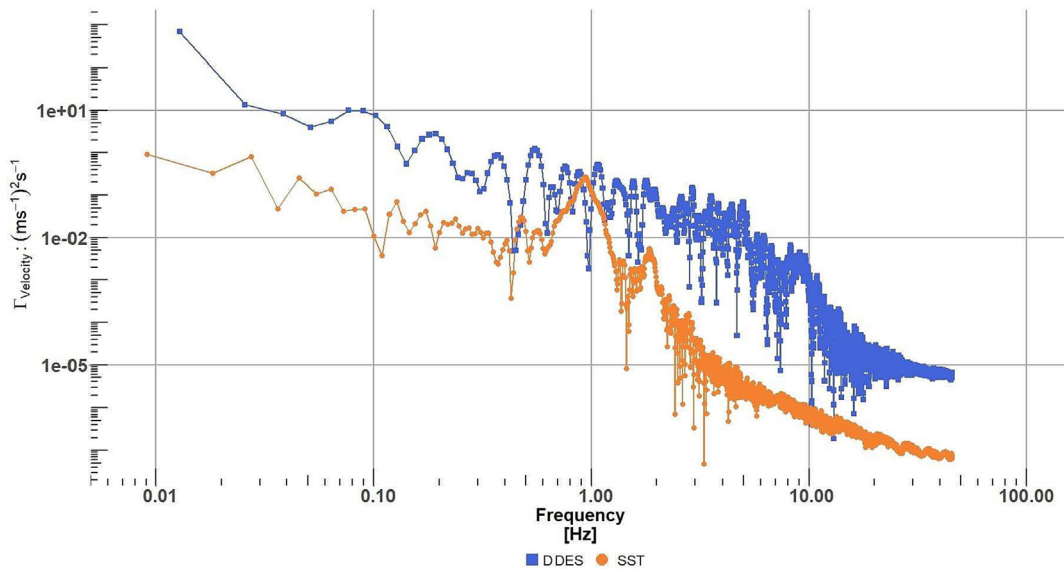


**FIGURE 25** Comparison of the power spectral density relative velocity for the DDES and SST model at  $r/R = 0.13$  for the spoiler case. The blue square (■) shows the 3D relative velocity results for the DDES model and the orange dot (●) shows the 3D relative velocity results for the SST model.

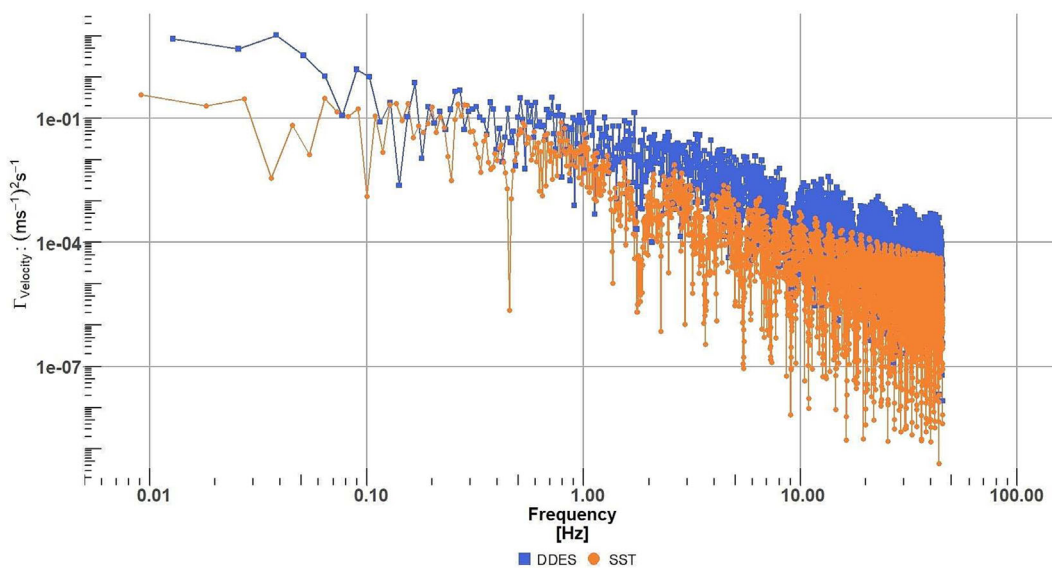


**FIGURE 26** Comparison of the power spectral density relative velocity for the DDES and SST model at  $r/R = 0.28$  for the spoiler case. The blue square (■) shows the 3D relative velocity results for the DDES model and the orange dot (●) shows the 3D relative velocity results for the SST model.

wake are well formed (Figure 21A,C), homogeneous in their size and with a proper alternation of the vortex sign. This results in a clear peak frequency. In the 3D wake, the vortices are not round (highlighted with black isocontours of the Q-criteria), not formed regularly and with a high vorticity level (in red and blue) between them (Figure 21B,D).

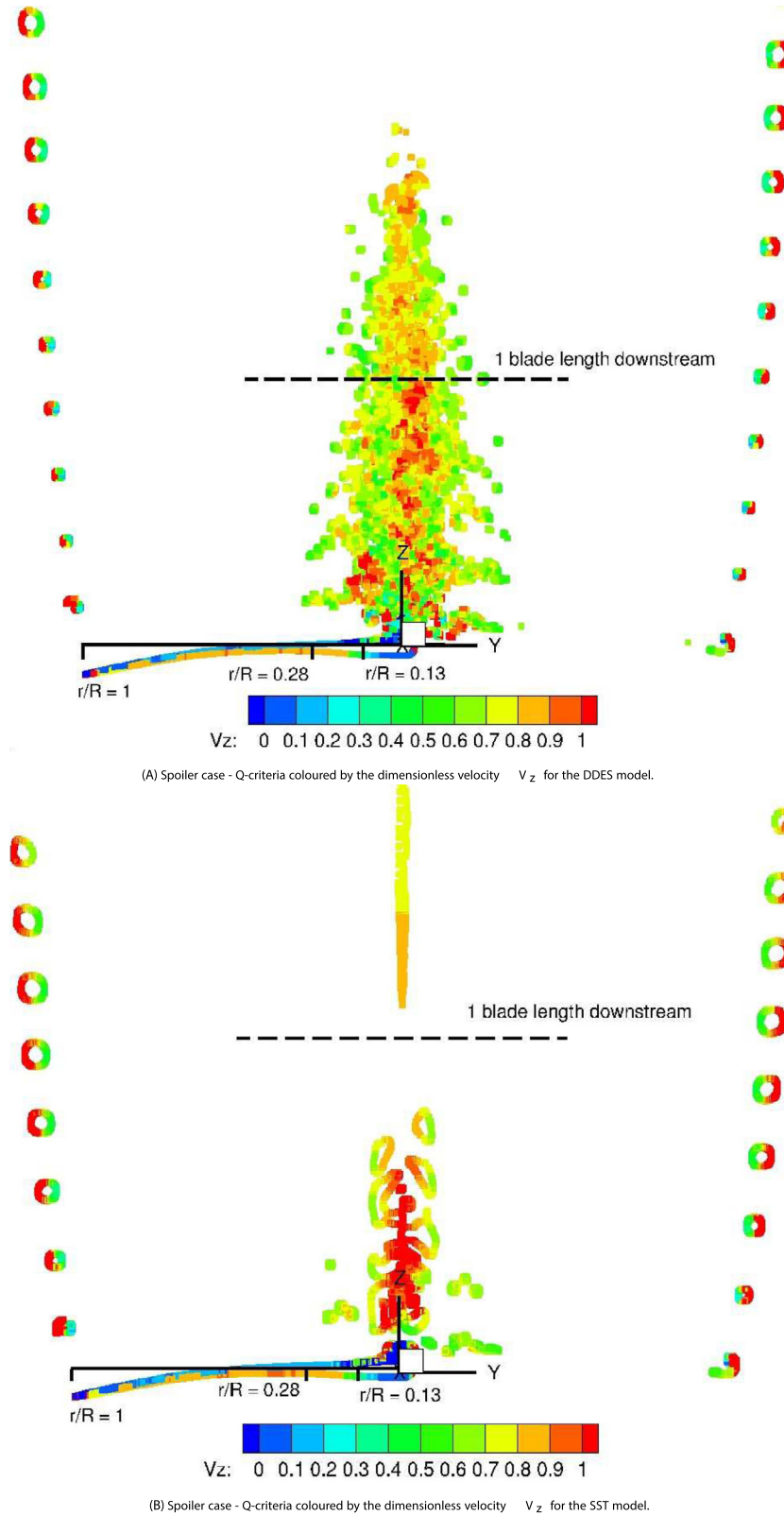


**FIGURE 27** Comparison of vortices in the wake of the turbine for different turbulence models.

Figure 22A,B compares the 2D and 3D spectrum of the relative velocity in the aerofoil's wake for both cases. "2D CL" refers to the lift coefficient calculated by integrating the pressure coefficient around the aerofoil from 2D CFD simulations. "2D Inflow" refers to the measured data through a probing point positioned in the wake of the 2D aerofoil. Similarly to the outcome when comparing the lift coefficients and wake velocity in 3D (see Figures 14 and 16), the no-spoiler case shows a good agreement in peak frequencies for the 2D and 3D simulations. However, in the spoiler case, the 2D simulation does not catch the first peak below 1 Hz, but detects the higher ones. It is probably due to the too large frequency step chosen in 2D.

Focusing now on the  $C_L$  spectrum, the differences between 2D and 3D organization without and with spoiler is mostly reflected by the decrease in the energy in the spectrum, while the VSF remains almost unchanged (see Figures 23 and 24). This validates the use of 2D simulations to compute VSF values in a first design approach regarding the fatigue evaluation introduced in Potentier et al.<sup>9</sup>

The investigation at the aerofoil scale shows a significant difference between 2D and 3D simulations on the pressure distribution and thus local aerofoil loads in the inboard area. These differences are found less important in the evaluation of the VSF for fatigue computation, even if the 2D simulations significantly overpredict the peak frequency energy.

### 6.3 | URANS–DDES

There are known difficulties associated to URANS model to simulate highly swirling flows that has led to the development of more advanced turbulence model, for example, delayed detached eddy simulation (DDES) model. DDES model combines the best aspects of LES and URANS model. Indeed, large eddy simulation (LES) is well known as a better model compared to the URANS model in terms of accuracy for highly separated flow, but its computational cost is high especially near the wall, in the viscous boundary layer. The best aspects of DDES is the hybrid calculation approach: URANS is applied near the wall and the LES model applied far from the body.

In previous results, the  $k-\omega$  SST URANS model (or SST model as later named) has been used. It can be extended easily in ISIS-CFD by selecting the DDES model. Only the blade equipped with the spoiler has been ran, due to the high CPU cost because of the finer mesh and smaller time step required. Figure 25 shows differences in the relative velocity wake spectrum at the radial position  $r/R=0.13$ . As expected, the energy in the spectrum is well distributed over all frequency values in DDES simulations, while the SST simulations has a single dominant frequency ( $\approx 1$ Hz). Regarding its use for fatigue analysis, the DDES presents a completely different excitation pattern. More investigations are necessary to draw any further conclusions, especially regarding the convergence of DDES simulations which needs to be improved. However, it is interesting to notice that, after the spoiler position both the SST and DDES model produce a similar spectrum as seen on Figure 26.

The DDES model is able to capture a much broader array of turbulence structure, which is confirmed by the presence of numerous vortices of different sizes in DDES simulations compared to simulations of the SST model in the inboard region of the rotor wake (see Figure 27A,B). It should be noted that these vortices are more persistent in the rotor wake for the DDES model than the vortices from the SST model.

## 7 | CONCLUSIONS

The current work highlighted the spoiler impact using 3D simulations. The findings can be summarized as follows: The addition of the spoiler influences the near wake by means of reducing the size of the cone region; however, its influence on the far wake velocity recovery is limited. Similarly, the induction area upstream the rotor is not impacted by the spoiler. The local inboard blade quantities however, that is, the axial and tangential induction and angle of attack, are very much impacted. The axial induction and the tangential induction increases, leading to a reduction of the local angle of attack. When analysing the flow locally, this can be explained by a redistribution of the pressure around the blade with the spoiler case. However, it cannot be due to a modification of the separation area nor by modification of crossflow region, which are almost identical in both cases. Local loads with a spoiler are increased, mostly due to the lift and drag increase following the pressure redistribution. A positive side effect is the more balanced loads in the chordwise direction. The counterpart is an increase of the flow oscillations with two major sources of excitation: The blade shedding frequency and the crossflow oscillations. These oscillations are found to be transferred to the structure through the lift variation. The energy content in the  $C_L$  spectrum is higher in the spoiler case despite the no-spoiler case having similar peak frequencies.

In 3D, the spoiler presence produces similar overall effect as in 2D simulations, with a redistribution of the pressure, an increase of the wake area, and the level of the lift oscillations, with no impact on the flow separation. However, major differences exist between 3D and 2D simulations at the aerofoil scale for inboard regions such as the wake and vortices organization and the presence of the cross-flow due to Coriolis effects.

At the aerofoil scale, for the no-spoiler case, the mean lift is significantly different between 2D and 3D simulations because of the crossflow benefit from Coriolis effects. Where the spoiler is installed, similar mean lift is observed between 2D and 3D simulations. Regarding the aerofoil wake unsteadiness, 3D simulations are found to significantly dampen the lift oscillations, leading to a significant decrease of the lift spectrum energy and thus on its transmission to the structure. Regarding the application to fatigue calculation, it is noted that the actual value of the VSF

has less impact than the actual aerodynamic coefficient amplitude. No significant modification of the peak frequency value is found, without and with the spoiler both in 2D and 3D.

To conclude this study, DDES simulations were briefly compared with SST model results. They present a broader frequency range in the blade inboard wake with a higher energy level than 3D URANS simulations. Such findings need to be investigated further as part of dedicated studies.

## AUTHOR CONTRIBUTIONS

Thomas Potentier performed the CFD preprocessing and postprocessing, calculations and analysis, and writing of the paper. Emmanuel Guilmineau performed CFD verification and helped set up the CFD model. Colin Le Bourdat and Arthur Finez provided feedback from the industrial point of view, and Caroline Braud helped with writing and proofreading previous versions of the manuscript and physical analysis of the results.

## ACKNOWLEDGEMENTS

The computations were performed using HPC resources from GENCI (Grand Equipement National de Calcul Intensif) (Grant A0112A13014), which is gratefully acknowledged.

## CONFLICT OF INTEREST STATEMENT

The authors declare no potential conflict of interests.

## DATA AVAILABILITY STATEMENT

The data that support the findings of this study are available from ENIGE Green. Restrictions apply to the availability of these data, which were used under license for this study. Data are available from the authors with the permission of ENGIE Green.

## ORCID

Thomas Potentier  <https://orcid.org/0000-0001-7213-0021>

## PEER REVIEW

The peer review history for this article is available at <https://www.webofscience.com/api/gateway/wos/peer-review/10.1002/we.2823>.

## REFERENCES

1. International Renewable Energy Agency. *Future of Wind Deployment, Investment, Technology, Grid Integration and Socio-economic Aspects*: International Renewable Energy Agency; 2019. <https://www.irena.org/publications/2019/Oct/Future-of-wind>
2. Pechlivanoglou G. *Passive and Active Flow Control Solutions for Wind Turbine Blades*. Ph.D. Thesis: Technische Universität Berlin; 2013.
3. Saleem Z. *Investigation of passive root flaps on HAWT*. Master's Thesis: TU Delft; 2019.
4. Bach AB. *Gurney flaps and micro-tabs for load control on wind turbines*. Ph.D. Thesis: Technische Universität Berlin; 2016.
5. Heejeon Im BK. Numerical analysis of the effect of vortex generator on inboard region of wind turbine blade. *J Renew Sustain Energy*. 2021;13(6): 63306.
6. Zhang Y, Ramdoss V, Saleem Z, Wang X, Schepers G, Ferreira C. Effects of root Gurney flaps on the aerodynamic performance of a horizontal axis wind turbine. *Energy*. 2019;187:115955.
7. Alber J, Soto-Valle R, Manolesos M, et al. Aerodynamic effects of Gurney flaps on the rotor blades of a research wind turbine. *Wind Energy Sci*. 2020; 5(4):1645-1662. <https://wes.copernicus.org/articles/5/1645/2020/>
8. Potentier T, Guilmineau E, Finez A, Bourdat CL, Braud C. High-Reynolds-number wind turbine blade equipped with root spoilers—part 1: unsteady aerodynamic analysis using URANS simulations. *Wind Energy Sci*. 2022;7(2):647-657. <https://wes.copernicus.org/articles/7/647/2022/wes-7-647-2022.html>
9. Potentier T, Guilmineau E, Finez A, Le Bourdat C, Braud C. High-reynolds-number wind turbine blade equipped with root spoilers—part 2: impact on energy production and turbine lifetime. *Wind Energy Sci*. 2022;7(4):1771-1790. <https://wes.copernicus.org/articles/7/1771/2022/>
10. Queutey P, Visonneau M. An interface capturing method for free-surface hydrodynamic flows. *Comput Fluids*. 2007;36:1481-1510.
11. Guilmineau E, Deng GB, Leroyer A, Queutey P, Visonneau M, Wackers J. Assessment of hybrid RANS-LES formulations for flow simulation around the Ahmed body. *Comput Fluids*. 2017;176:302-319. <https://linkinghub.elsevier.com/retrieve/pii/S0045793017300051>
12. Guilmineau E, Deng GB, Leroyer A, Queutey P, Visonneau M, Wackers J. Numerical simulations for the wake prediction of a marine propeller in straight-ahead flow and oblique flow. *J Fluids Eng*. 2018;140(2):21111. <https://asmedigitalcollection.asme.org/fluidsengineering/article/doi/10.1115/1.4037984/374183/Numerical-Simulations-for-the-Wake-Prediction-of-a>
13. Dambine G. *Impact of Blade Ageing on Wind Turbine Production*. Master's Thesis: European Master in Renewable Energy; 2010.
14. Rhie CM, Chow WL. A numerical study of the turbulent flow past an airfoil with trailing edge separation. *AIAA J*. 1983;21(11):1525-1532.
15. Issa RI. Solution of the implicitly discretised fluid flow equations by operator-splitting. *J Comput Phys*. 1986;62(1):40-65.
16. Wackers J, Deng G, Guilmineau E, Leroyer A, Queutey P, Visonneau M. Combined refinement criteria for anisotropic grid refinement in free-surface flow simulation. *Comput Fluids*. 2014;92:209-222. <https://linkinghub.elsevier.com/retrieve/pii/S0045793013005112>

17. Wackers J, Deng G, Guilmineau E, et al. Can adaptive grid refinement produce grid-independent solutions for incompressible flows? *J Comput Phys*. 2017;344:364-380. <https://linkinghub.elsevier.com/retrieve/pii/S0021999117303650>
18. Potentier T, Guilmineau E, Finez A, Le Bourdat C, Braud C. *Comparison Between 3D and 2D CFD Unsteady Simulations of the Danaero Blade*: 25 ième Congrès Français de Mécanique; 2022.
19. Simley E, Angelou N, Mikkelsen T, Sjöholm M, Mann J, Pao LY. Characterization of wind velocities in the upstream induction zone of a wind turbine using scanning continuous-wave lidars. *J Renew Sustain Energy*. 2016;8(1):13301.
20. Branlard ESP, Meyer Forsting AR. Using a cylindrical vortex model to assess the induction zone in front of aligned and yawed rotors. In: EWEA Offshore 2015 Conference. European Wind Energy Association (EWEA); 2015:1-11.
21. Troldborg N, Meyer Forsting AR. A simple model of the wind turbine induction zone derived from numerical simulations. *Wind Energy*. 2017;20(12):2011-2020.
22. Benard P, Viré A, Moureau V, et al. Large-eddy simulation of wind turbines wakes including geometrical effects. *Comput Fluids*. 2018;173:133-139.
23. Tossas LAM, Leonardi S. Wind Turbine Modeling for Computational Fluid Dynamics: December 2010 - December 2012. NREL/SR-5000-55054, 1089598, NREL; 2013.
24. Sørensen JN, Mikkelsen RF, Henningson DS, Ivanell S, Sarmast S, Andersen SJ. Simulation of wind turbine wakes using the actuator line technique. *Philosoph Trans R Soc A: Math Phys Eng Sci*. 2015;373(2035):20140071.
25. Hansen M. *Aerodynamics of Wind Turbines*. 3rd ed. Routledge; 2015.
26. Burton T, ed. *Wind energy: Handbook*. J. Wiley; 2001.
27. Hansen MOL, Sørensen NN, Sørensen JN, Michelsen JA. Extraction of lift, drag and angle of attack from computed 3-d viscous flow around a rotating blade. In: 1997 European Wind Energy Conference Irish Wind Energy Association; 1998:499-502.
28. Rahimi H, Schepers G, Shen WZ, et al. Evaluation of different methods for determining the angle of attack on wind turbine blades with CFD results under axial inflow conditions. *Renew Energy*. 2018;125:866-876. <http://arxiv.org/abs/1709.04298>
29. Herráez I, Akay B, van Bussel GJW, Peinke J, Stoevesandt B. Detailed analysis of the blade root flow of a horizontal axis wind turbine. *Wind Energy Sci*. 2016;1(2):89-100. <https://www.wind-energ-sci.net/1/89/2016/>
30. Herráez I, Daniele E, Schepers JG. Extraction of the wake induction and angle of attack on rotating wind turbine blades from PIV and CFD results. *Wind Energy Sci*. 2018;3(1):1-9.
31. Chow R, van Dam CP. Verification of computational simulations of the NREL 5 MW rotor with a focus on inboard flow separation: computational simulations of the NREL 5 MW rotor. *Wind Energy*. 2012;15(8):967-981.
32. Mo J-O, Lee Y-H. CFD Investigation on the aerodynamic characteristics of a small-sized wind turbine of NREL PHASE VI operating with a stall-regulated method. *J Mech Sci Technol*. 2012;26(1):81-92.
33. Potentier T. R6 uy and wssy. Copernicus Publications. Last accessed: 07 Sep 2022. <https://doi.org/10.5446/58973>; 2022.
34. Potentier T. R6 qcriteria and vorticity. Copernicus Publications. Last accessed: 07 Sep 2022. <https://doi.org/10.5446/58972>; 2022.
35. Islam S-U, Manzoor R, Islam Z-U, Kalsoom S, Ying ZC. A computational study of drag reduction and vortex shedding suppression of flow past a square cylinder in presence of small control cylinders. *AIP Advances*. 2017;7(4):45119.
36. Corten GP. Flow Separation on Wind Turbine Blades. *Ph.D. Thesis*: Universiteit Utrecht; 2001.
37. Sicot C, Devinant P, Loyer S, Hureau J. Rotational and turbulence effects on a wind turbine blade. Investigation of the stall mechanisms. *J Wind Eng Industr Aerodyn*. 2008;96(8-9):1320-1331.

**How to cite this article:** Potentier T, Guilmineau E, Finez A, Le Bourdat C, Braud C. High Reynolds number unsteadiness assessment using 3D and 2D computational fluid dynamics simulations of a thick aerofoil equipped with a spoiler. *Wind Energy*. 2023;26(7):668-690. doi:10.1002/we.2823